

Copper Chelation Induces Morphology Change in Mitochondria of Triple-Negative Breast Cancer

ChiaHung Lee, Zhen Xiao, Irene Lim, Ting Wang, Parisa Aghaei, Peter J. Burke,* and Jianghong Rao*

Cite This: <https://doi.org/10.1021/jacsau.5c00035>

Read Online

ACCESS |

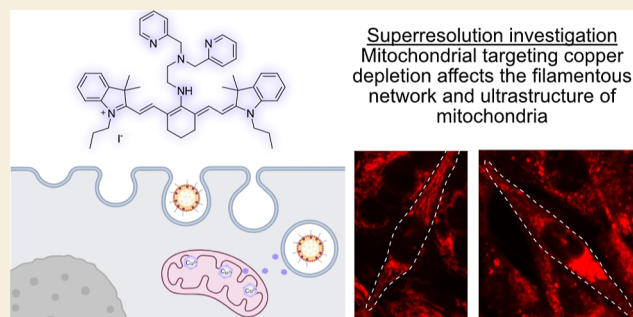
Metrics & More

Article Recommendations

Supporting Information

ABSTRACT: Recent studies implicate mitochondria playing a key role in the cellular response to copper depletion therapy; however, evidence has been indirect and downstream, and the initial target of chelation remains to be defined. Here, we show, using super-resolution voltage and structure imaging microscopy, that copper chelation directly affects mitochondria morphology (causing fragmentation of the filamentous network) and ultrastructure (causing internal cristae remodeling). When triple-negative breast cancer cells are treated with a mitochondria-targeting copper chelator, mitochondria undergo an irreversible change in morphology from tubular to spherical. This process can be prevented by the addition of exogenous copper during the treatment. We find that a tailor-designed chelating agent with positive charges to target mitochondrial electrostatics localizes inside the mitochondrial cristae in a voltage-dependent manner. On pharmacological induction of membrane potential collapse, the chelator is dispersed while the mitochondrial cristae structure is preserved. These results indicate that voltage-dependent localization/targeting of the copper chelator in mitochondrial cristae plays a key role in its cytotoxicity.

KEYWORDS: copper chelation, mitochondrial morphology, mitochondrial fragmentation, superresolution microscopy



Superresolution investigation
Mitochondrial targeting copper
depletion affects the filamentous
network and ultrastructure of
mitochondria

INTRODUCTION

Interest in the role of metals in biology has exploded over the past decade. Copper has been implicated in a wide variety of biological processes, such as mitochondrial respiration,¹ metabolism,² and inflammation.³ As copper is a toxic aqueous metal ion, its tight regulation in biology has been extensively studied.^{4–6} Copper regulation occurs through a poorly understood network of protein complexes, so much so that it is estimated that in any given cell, only one copper atom is unbound;⁷ the rest are complexed with highly regulated “copperome” proteins.

Recently, the role of copper in mediating cancer has garnered attention.^{7–10} It has been noted that tumors require higher levels of copper compared to healthy tissue.¹¹ Since copper is involved in both cell proliferation and cell death pathways, the relationship between disruption of the bioavailable and bound copper pools and cancer outcomes is extremely complex.¹² Indeed, copper chelation therapy based on tetrathiomolybdate (TTM) has been in clinical trials for preventing relapse of breast cancer.^{13,14}

To improve copper chelation therapy, one of our laboratories has designed, synthesized, and tested the downstream metabolic and cytotoxic/therapeutic effects of a custom-designed small molecule chelator specifically targeted to localize at, near, or in mitochondria: copper depleting moiety (CDM) (Figure 1A).¹⁵ CDM has two tailor-designed

moieties fused on the cyanine dye backbone: (1) it chelates copper (Cu) ions using moiety dipyrpyridylamine; (2) it has a distributed positive charge, making it both membrane permeable and responsive to potential differences (voltages) across the membrane. This led us to hypothesize that it would be taken up in large quantities inside mitochondria: since the mitochondrial membrane potential is ~ 150 mV, 6 times kT , one can anticipate an $e(150 \text{ mV}/kT) \sim 500$ -fold increase of CDM concentration inside the mitochondrial matrix. Some researchers have found higher membrane potential in cancer cells and postulated that it could enhance toxicity to cancer relative to normal cells.¹⁶ Our initial studies found evidence of CDM colocalization with standard confocal microscopy, but we did not investigate the localization of CDM within the mitochondria nor its effect on mitochondrial ultrastructure.

In our prior work,¹⁵ we studied in detail the copper chelating effect of CDM on both mitochondrial function in cells and survival rate in animal models. We hypothesized that disrupting this copper source in mitochondria would be an

Received: January 13, 2025

Revised: April 17, 2025

Accepted: April 18, 2025

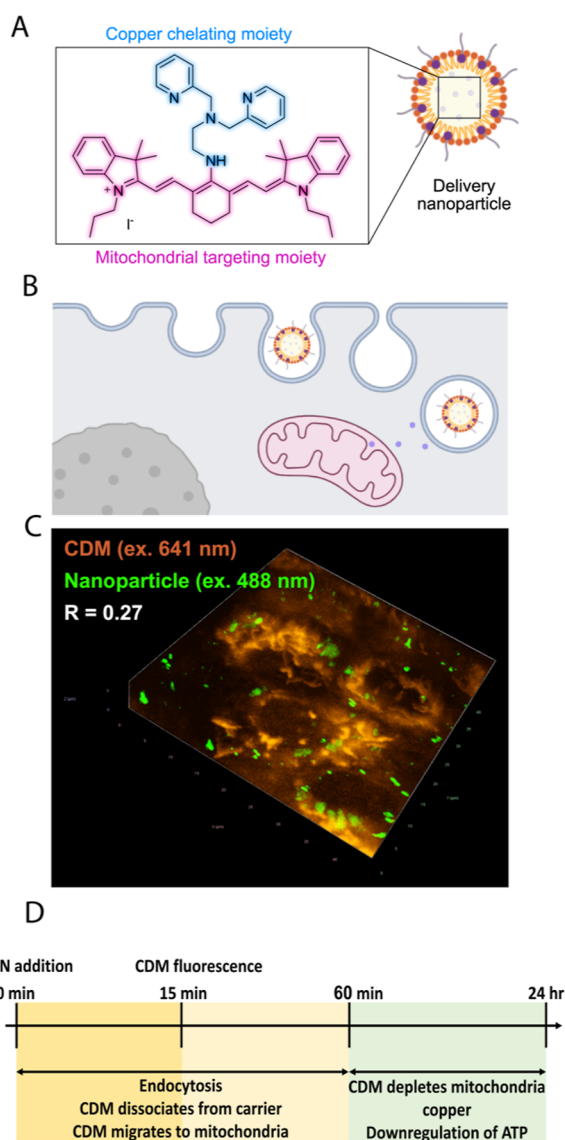


Figure 1. Colocalization of CDM in cells with mitochondria. (A) CDM and CDN design. (B) The CDN is taken up by cells, and then the CDM is released. Free CDM is localized in the mitochondria. (C) Image of stained mitochondria with 3D z stack in untreated cells for reference. MDA-MB-231 cells were treated with $1 \mu\text{M}$ CDM (orange) encapsulated in a polymer carrier (green, ex. 488 nm, em. 450–561 nm) for 30 min. The image is a Z-stack of the field of view. The Pearson's correlation coefficient = 0.27. (D) Timeline of CDN uptake and CDM mitochondria targeting.

effective strategy for treating diseases such as triple-negative breast cancer (TNBC). To improve the serum stability of CDM and enhance tumor delivery, we formulated CDM into semiconducting polymer nanoparticles as CDM-laden nanoparticles [copper depleting nanoparticles (CDNs)]. When we applied CDN to a mouse TNBC model, 50% of mice survived past the end of the study (68 days), as compared to the control group (median survival of 25 days). A similar effect has been demonstrated in TNBC models using a different copper chelator as well.¹⁷ Another study reports the use of a polymeric copper chelator together with an agonist of TLR7 and TLR8 to treat metastatic breast cancer, but there was no study of the effect on the mitochondria copper and structure.¹⁸

The biochemical characterization of CDM in cells also yielded insight into the mechanism. CDM inhibited cytochrome C oxidase (COX) in mitochondria by 50% in TNBC cells.¹⁵ This resulted in mitochondrial oxidative phosphorylation activity decreases and a metabolic switch to glycolysis, leading to a 50% decrease in adenosine triphosphate (ATP) generation. Driven by compromised mitochondrial membrane potential, decreased endogenous antioxidants, and elevated oxidative stress, TNBC cells eventually undergo apoptosis.

However, there remained several unanswered questions in our initial work: does the CDM enter the mitochondria or operate only on the surface of the cytoplasm side? What role does the nanoparticle cargo carrier play and does it insert into the mitochondria? What role does the membrane potential play and does it attract and concentrate the CDM as designed to? In this work, we set out to answer these questions, exploiting our recent advances¹⁹ in biophysical understanding of charged small molecule distribution in mitochondria as voltage imaging agents with super-resolution microscopy. In the process, we also discovered that the CDM treatment causes mitochondrial structure changes (fragmentation), either upstream or concurrent with our prior measured metabolic shifts and well upstream of apoptosis, thus clearly implicating mitochondrial localization of copper chelation as a primary role in its mechanism of action.

RESULTS

CDM Accumulates in Mitochondrial Cristae

Our prior work has shown that CDM-laden nanoparticles CDN are taken up by various cell lines. We found CDM colocalizes with mitochondria at the resolution of confocal microscopy, but we did not know the fate, i.e., the final location of the CDN in the cell or CDM with respect to the mitochondrial ultrastructure. Here, extending our prior work to further explore the mechanism, pathway, and final location of CDM, we find that CDN is taken up via endocytosis, followed by the release of CDM from the CDN matrix. We find that CDM is taken up inside the mitochondria and localized in the cristae at the cristae membranes. This finding is made possible by our expertise with super-resolution imaging of mitochondrial voltages.¹⁹ Confocal microscopy alone would not have been able to resolve this, hence there was our lack of knowledge of this effect in our prior work.¹⁵ The cartoon in Figure 1 shows our current model.

We first characterized the behavior of CDM, our mitochondrial copper chelator, in MDA-MB-231 cells (Figure 1A). Our first observation is that the ~ 100 nm diameter CDN polymer nanoparticle “carriers” are aggregated and not colocalized with CDM. The Z-stack in Figure 1C shows the CDM localized around the nucleus in a pattern similar to that expected of mitochondria. Quantitatively, the localization coefficient is 0.27, indicating that the CDM has become dissociated from the CDN carrier. In order to investigate this further, we next imaged more carefully mitochondria and CDM location, as described next.

In Figure 2A, we show that CDM and mitochondria are closely localized. The CDM is red natural fluorescence; mitochondria are labeled with MitoTracker green (MTG), which indicates the mitochondrial structure. The Pearson factor is 0.82, indicating strong colocalization. In order to further investigate the nature of the colocalization, we labeled

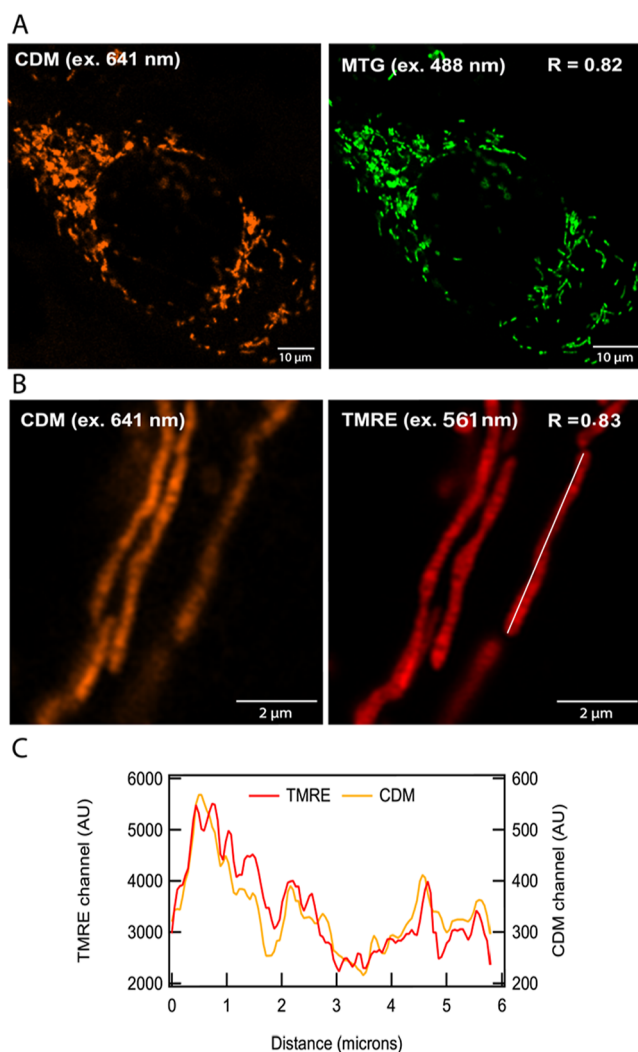


Figure 2. Colocalization of CDM in mitochondrial cristae. (A) MDA-MB-231 cells were treated with 1 μM CDM and 100 nM MitoTracker Green for 15 min. The Pearson's correlation coefficient, calculated between the CDM channel (orange, ex. 641 nm, em. 642–700 nm) and MTG channel (green, ex. 488 nm, em. 450–561 nm), is 0.87. (B) High-resolution microscopy of MDA-MB-231 treated with 100 nM of CDM (orange, ex. 641 nm, em. 642–700 nm) and 10 nM of TMRE (red, ex. 561 nm, em. 561–700 nm) for 15 min. Pearson's correlation coefficient = 0.83. (C) Line profile showing colocalization of CDM and TMRE at the mitochondrial cristae.

mitochondria with tetramethyl rhodamine ethyl ester (TMRE) (a voltage-sensitive dye) and observed strong colocalization of TMRE and CDM (Figure 2B,C) (Pearson value at 0.83). Additional images of independent experiments are presented in Figure S5. The super-resolution images clearly indicated that CDM is closely bound to the mitochondrial inner cristae membrane, just as the voltage dye TMRE is. When interpreted in light of our recent detailed biophysical model of how TMRE labels mitochondrial cristae voltages,¹⁹ we discover that the CDM binds to the membrane. This provides strong evidence for our hypothesis that the positive charge on the CDM targets the mitochondria based on the mitochondria's large membrane potential.

CDM Localization is Dependent on the Membrane Potential

As shown in Figure 3, to further test the hypothesis of mitochondria targeting CDM, we next imaged the mitochondria CDM and MTG fluorescence intensity when the membrane potential was pharmacologically collapsed with carbonyl cyanide-*p*-trifluoromethoxy phenylhydrazone (FCCP), an uncoupling agent that disrupts ATP synthesis by transporting hydrogen ions through the mitochondrial membrane. The fluorescence intensity of the CDM signal dropped by 88% after treatment with FCCP, while there were no significant differences in the MTG fluorescence (Figure 3C). As MTG labels mitochondria covalently,²⁰ the loss of membrane potential should not impact the fluorescence of the MTG. In the case of CDM, however, the loss of membrane potential impacts the fluorescence of CDM. This confirms our hypothesis that CDM is localized inside mitochondria cristae membranes in a voltage-dependent manner, similar qualitatively and quantitatively to voltage dye TMRE.¹⁹

CDM Induces Irreversible Mitochondria Fragmentation

In order to further understand the toxicity of CDM, we opted to study long-term changes in cellular health by microscopy. While there are many metrics to assess cytotoxicity, in our work we noticed that the earliest observable deleterious effect of the CDM/CDM exposure regimen was mitochondrial shape change. Further, toxic effects such as apoptosis and metabolic shifts occurred downstream in time from this shape change. Furthermore, the shape change was a readily apparent and robust phenomenon.

We use sphericity, calculated as the perimeter-to-area ratio, as an approximation of mitochondrial health. This metric has been used to assess mitochondrial "damage" from chemical and phototoxic effects in other contexts and is generally agreed upon as one metric for assessing toxicity in cells.^{21–27} A value close to 1 indicates a perfect circle, representing an unhealthy mitochondrion. A value close to 0 indicates a tubular shape, representing a healthy mitochondrion. We used an open-source Github algorithm developed in-house²¹ to quantitatively assess mitochondrial "damage" in an operator-independent fashion.

24 h of incubation with CDM led to mitochondrial morphological changes, transitioning from tubular to circular shapes (Figure 4). For cells incubated with 1 μM CDM for 24 h, the mitochondria sphericity increased to 0.7–1.0, indicating that the majority of the mitochondria turned into circular shapes. We note that this morphological alteration is CDM concentration dependent. To determine if this morphological alteration is part of the typical fission and fusion behavior of mitochondria, we washed the cells after 24 h of CDM incubation and refilled them with fresh medium to observe further mitochondrial behavior. After 24 h between washing and observation to allow equilibrium, we note that the mitochondria do not return to tubular shapes and remain spherical. In all of our experiments, the transition to spherical is irreversible.

Copper Addition Prevents the Mitochondria from Morphological Changes

Given the morphological changes observed in mitochondria, we hypothesized that the interaction of CDM with copper is driving these changes. If CDM indeed affects toxicity in cells by chelating with copper in mitochondria and disrupting

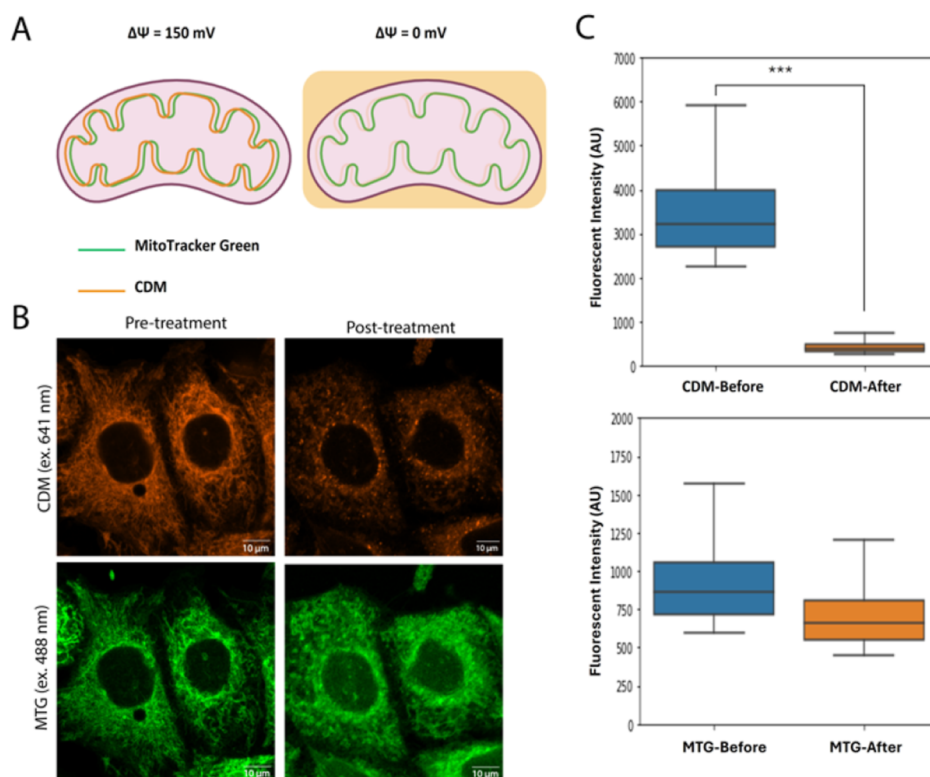


Figure 3. CDM labels mitochondria in a voltage-dependent manner. (A) Schematic of mitochondria staining by CDM and MitoTracker Green before and after FCCCP depolarization. (B) MDA-MB-231 cells were treated with 100 nM MitoTracker Green for 15 min and then incubated with 1 μM CDM for 30 min. The cells were then depolarized by 10 μM FCCCP addition. Cells were imaged 5 min after FCCCP treatment. Scale bar = 10 μm . (C) Quantification of the fluorescence intensities by ImageJ. Fluorescence intensity of FCCCP-treated cells dropped by over 88% in the CDM channel. *** = $p < 0.05$.

oxidative phosphorylation, then exogenous copper should impact the toxicity.

In order to test this hypothesis, we performed an experiment in which cells were treated with 1 μM CDM for 30 min and then treated with copious amounts of exogenous copper(II) (10 μM) (Figure 5). This amount of copper would overwhelm the binding sites of CDM, thus mitigating any effect of CDM on the Cu concentration in the cell.

The cells were observed up to 2 h after copper addition. We found that cells that had been pretreated with CDM displayed mitochondrial fragmentation (consistent with the initial results presented above), whereas those exposed to copper retained their filamentary structure (Figure 5). To quantify the observed differences in mitochondrial morphology, we performed an image analysis that included length, width, branching count, and sphericity measurements. Compared to the no-copper condition, copper-treated cells had significantly more prolonged and broader mitochondria and increased considerably branching in the mitochondrial network. Additionally, mitochondrial sphericity was significantly reduced after copper treatment, which indicates a shift toward more elongated and filamentary structures. These morphological metrics were extracted using ImageJ-based quantification (for length, width, and branching) and the published mitoAnnotation algorithm (for sphericity). Statistical comparisons also showed these significant differences and supported the conclusion that exogenous copper improves the mitochondrial structure after chelation-induced damage. All data and methods used are provided in the Supporting Information (Tables S3–S5 and Figures S16–S18).

Although we know from in vitro studies that CDM chelates Cu, we confirmed independently in this work that CDM chelates Cu in cells under the conditions used in this paper. In order to confirm that CDM was indeed complexing copper, we performed a fluorescent experiment to determine the amount of copper bound to CDM. We pretreated cells with CDM and then added excess copper (Figure S4) or a control solution. When copper is complexed to CDM, the fluorescence intensity decreases through a metal-to-ligand photoinduced electron transfer mechanism.¹⁵ This effect was observed in the cells; fluorescence intensity decreased by over 90% in the first 30 min after copper addition (Figure S4). These results clearly demonstrate the copper chelation by CDM and the role of Cu chelation in cytotoxicity, when neutralized by copious exogenous Cu, prevents mitochondrial structure change (fragmentation).

Toxicity Is Driven by Mitochondrial Accumulation of a Copper Chelator

In order to elucidate and confirm the relative roles of the mitochondrial targeting and Cu chelating moieties of our tailor-designed CDM, we decided to compare the effects of related compounds that have only one moiety but not the other moiety (Table 1). CDM comprises two components, a mitochondrial-targeting cyanine dye and a copper chelator. To systematically understand how the two components influence toxicity, we conducted structure–property studies in which the cyanine dye precursor, IR780, and a nonmitochondrial targeting copper chelator, ATN-224, were compared to CDM using an MTT (3-(4,5-dimethylthiazol-2-yl)-2,5-diphenyltetrazolium bromide) cell viability assay.

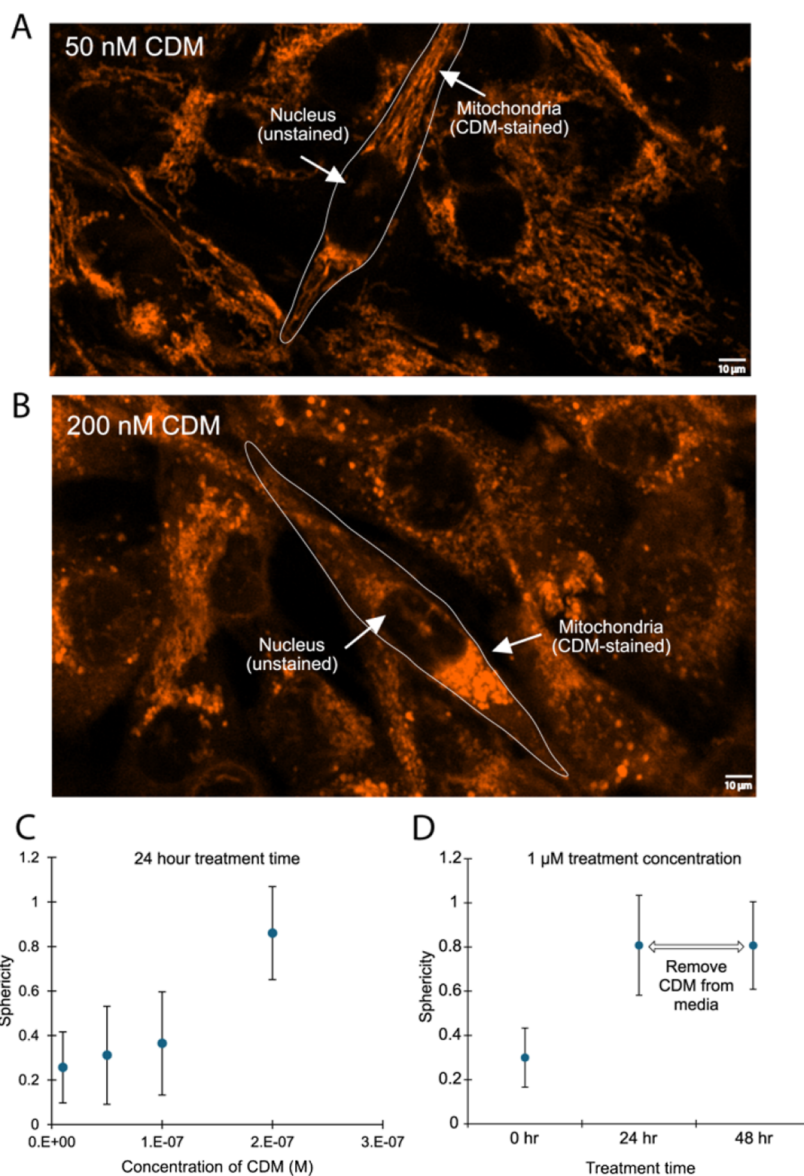


Figure 4. Mitochondrial morphological changes induced by CDM. MDA-MB-231 cells were incubated with various concentrations of CDM for 24 h and imaged in the CDM channel (ex. 641 nm, em. 642–700 nm). Representative images at 50 (A) and 200 nM (B) show mitochondrial fragmentation. Scale bar = 10 μm . (C) Sphericity vs CDM concentration after 24 h of incubation. (D) Sphericity vs time at 1 μM CDM, showing sphericity does not recover after exposure and subsequent removal from the media.

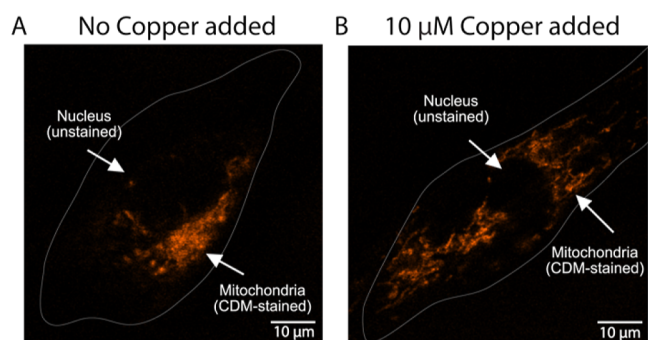
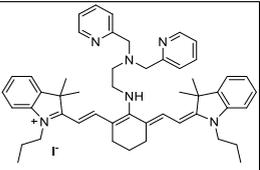
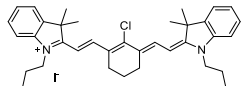
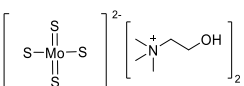


Figure 5. Addition of copper blocks phenotype alteration. (A,B) MDA-MB-231 cells were incubated with 1 μM CDM for 30 min, washed, then treated without (A) or with (B, control) 10 μM copper for 2 h. The cells were imaged on the CDM channel (ex. 641 nm, em. 642–700 nm). Scale bar = 10 μm .

IR780 has virtually the same structure as CDM but lacks the Cu-chelating dipyrindyl amine groups; it is charged, and the charge is distributed, making it likely a mitochondria-targeting small molecule. In comparison, ATN-224 has no such mitochondria-targeting apparatus and yet operates as a Cu chelator. In Figure 6, we find that the inhibitory concentration at 50% (IC_{50}) of CDM is the lowest of all three small molecules, with CDM being the most potent cytotoxin among the three species.

The fact that IR780 was also toxic is not a surprise. In general, it is well-known that, at relatively high concentrations, lipophilic cations can have cytotoxic effects unrelated to the Cu chelation we found in CDM. This is consistent with other cytotoxic effects²⁸ well-known from lipophilic cations and presumably due to the lower membrane potential caused by the cations. At high enough concentrations, the accumulation of lipophilic cations creates a short circuit through the membranes of cells and mitochondria and therefore partially

Table 1. Chemicals Studied in This Work and Their IC₅₀ Values in MBA-MD-231 Cells

Compound			
	CDM	IR780	ATN-224
Cu chelating	Yes	No	Yes
Mitochondria targeting	Yes	Yes	No
IC ₅₀	4.8 ± 0.2 μM	12.8 ± 0.7 μM	>100 μM
Causes ΔΨ reduction	Yes	Yes	No

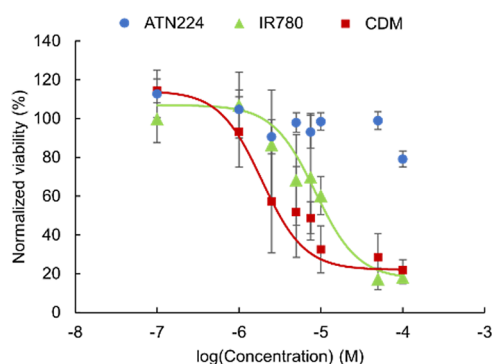


Figure 6. Cell viabilities of MBA-MD-231 cells treated with ATN-224, IR780, or CDM. IC₅₀ of ATN-224 > 100 μM; IC₅₀ of CDM = 4.8 ± 0.2 μM; and IC₅₀ of IR780 = 12.8 ± 0.7 μM.

dissipates the membrane potential.^{29,30} Even the dye TMRE is known to have cytotoxic effects, which is why it is used at low concentrations, typically 10 nM.^{31,32} However, CDM has cytotoxic effects that occur at much lower concentrations than other cationic species such as TMRE and IR780, and it can be prevented via Cu addition, as we have shown above. ATN-224 cytotoxicity has a much larger IC₅₀. This indicates that mitochondrial targeting and Cu chelation combine to make CDM the most cytotoxic of the three molecules.

In order to further elucidate the mechanism of toxicity, we confirmed that both ATN-224 and IR780 also cause mitochondrial fragmentation and sphericity at doses above IC₅₀ (see Supporting Information Figure S11). Furthermore, we assayed the mitochondrial membrane potential with TMRE for both ATN-224 and IR780. The fluorescence signal of TMRE remained the same between time points, suggesting the membrane potential is not impacted by ATN-224 treatment. In contrast, for IR780, there was a substantial drop in membrane potential. This indicates that the mechanism of ATN-224 is not related to membrane potential, but the mechanism of IR780 is related. This is consistent with the hypothesis that lipophilic cations cause toxicity in part through the reduction in membrane potential. Taken together, these observations support the model that the mechanism of toxicity is Cu chelation in a mitochondria-targeted way.

Mitochondrial Morphology Change is Not Attributable to Phototoxicity

In recent years, the observations of phototoxicity have clearly shown that excess optical pumping can cause mitochondria to convert from the tubular form to the spherical form. The term “sphericity” has been developed as a surrogate for mitochondrial damage caused by phototoxicity. To ensure that the illumination energy dose during imaging did not cause phototoxic effects, we estimated the energy dose for each imaging condition based on laser power, pixel dwell time, scan area, and total number of pixels, assuming uniform illumination across the scanned region (see Supporting Information Table S2).

A phototoxicity threshold of approximately 2 J/cm² has been reported for MitoTracker Red (CMXRos) in confocal imaging.³³ Subsequent studies,²¹ emphasized that phototoxicity does not have a uniform threshold but depends on dye chemistry, excitation wavelength, light intensity, and exposure duration. These findings are consistent with previous reports,³³ which directly compared multiple mitochondrial dyes and showed that MitoTracker Green (MTG) and TMRE exhibit significantly lower phototoxicity than CMXRos under the same light conditions. More recent studies²¹ independently confirmed the low phototoxic response of MTG and TMRE under long-term imaging conditions.

We therefore compared our calculated energy doses to those used in the previous study²¹ and found that all measured values in our study were significantly below those associated with phototoxic responses. We conclude that the observed changes in mitochondrial morphology are solely due to the chemical effect of CDM treatment and are not attributable to phototoxicity induced by imaging.

DISCUSSION

Mitochondrial Sphericity as an Assay for Mitochondrial Damage

Mitochondrial ultrastructure has been known to change in response to the metabolic needs of a cell ever since Hackenbrock first studied transmission electron microscopy (TEM) images of liver mitochondria under various conditions in the 1960s.^{34,35} The general consensus is that increased cristae density provides a larger surface for the electron transport chain to synthesize the increased ATP demands of a cell. Such a cristae growth/shrinkage is considered a natural, healthy process of cell adaptation and occurs through

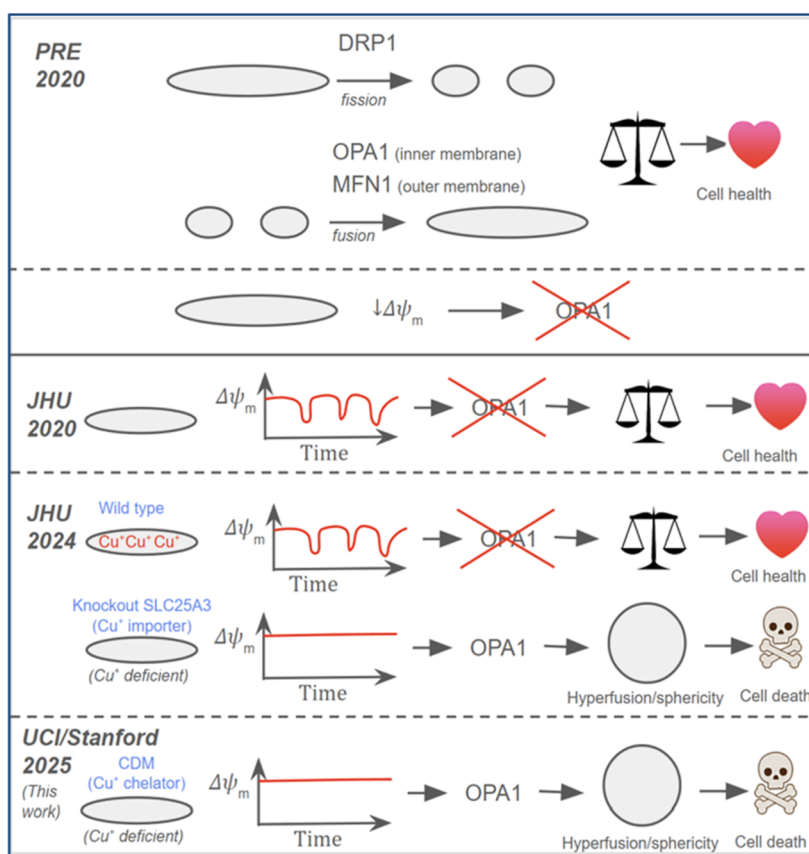


Figure 7. Top panel: pre-2020 understanding of the balance between fission and fusion. It was also known that reduced mitochondrial membrane potential caused degradation of OPA1. Next panel: JHU in 2020⁶³ showed that transient flickering of the mitochondrial membrane potential helped maintain the balance between fission and fusion. JHU in 2024⁶¹ showed that Cu⁺ is required for this process, and Cu⁺ deficient mitochondria (caused by knockout of the Cu⁺ importer SLC25A3) had less flickering and were hyperfused and spherical in morphology, and resulted in lower ATP production, apoptosis, and ultimately cell death. Bottom panel: proposed mechanism for the findings of this work, where CDM Cu⁺ chelation also causes sphericity (as observed here) and ultimately cell death.

upregulation and/or downregulation of lipid and other synthesis processes and therefore is a multihour process. Recently, with the advent of super-resolution microscopy and other techniques, there has been a resurgence of interest in mitochondrial ultrastructure,^{36–42} culminating in our recent work showing superresolution imaging of cristae of vital-isolated mitochondria in response to different chemical environments.¹⁹ However, these studies generally are not in response to stress, toxicity, or other insults.

Mitochondrial “sphericity” is one parameter of mitochondrial damage that has been associated with aging, apoptosis, and chemical insults. Progressive sphericity has been observed using a variety of imaging systems, including stimulated emission depletion (STED) microscopy and structured illumination microscopy (SIM), in association with photobleaching and phototoxicity. The transformation of mitochondria from tubular to spherical was irreversible.^{33,43,44} Thus, the general consensus from these studies is that mitochondrial sphericity is indicative of some sort of damage, but the exact downstream consequences are unknown.

Contrast that with our recent findings that mitochondria isolated from cells via mechanical lysis and differential centrifugation for study in suspensions, long a mainstay research program, results in spherical mitochondria which, apparently, are completely normal and healthy, in that they respond to substrates and inhibitors of the electron transport chain, respire, and produce ATP.⁴⁵ This may be a very

abnormal situation since the mitochondria are removed from the cytosol, which does not occur naturally and removes the cytosolic biochemical and mechanical environment.

Finally, stem cell mitochondria, which are metabolically dormant until differentiation, tend to have a very loose cristae structure, as well as a spherical morphology.^{22,46,47} These change into cristae-dense, tubular mitochondria on differentiation; therefore, the spherical morphology is reversible and not indicative of malady or poor “health” of the mitochondria.

One very interesting question in the context of this work is the role of mitochondrial sphericity in apoptosis. In the apoptosis pathway, it is generally believed that the release of cytochrome C (CytC), which resides inside the cristae of mitochondria,^{48–52} is the point of no return in the cell death pathway, and hence is highly regulated and a clear target for pharmacological manipulation⁵³ with promising success in the clinic and dozens of current clinical trials.^{54,55} However, the exact mechanism by which CytC escapes the tight cristae, stapled together by optic atrophy protein 1 (OPA1), is unknown.⁵⁶ In fact, controversy about the size of the constriction through which CytC must escape persists to this day. We have shown it corresponds also to proton efflux (pH change) and occurs commensurate with and may be caused by membrane potential decline.^{57,58}

Role of Copper in Mitochondrial Morphology and Function

In this work, we use sphericity as a stand-in for mitochondrial health. Compromising mitochondrial health is one of the early indicators of apoptosis, and we quantify the sphericity after different treatments to understand how cellular health is impacted. We observed the adverse effects of CDM on mitochondrial morphology, which worsened with time and concentration and could be prevented with copper addition. If CDM interacts with one of the Cu nuclei in cytochrome C oxidase (COX), this could lead to the disruption of the electron transport chain in mitochondria. Indeed, a 24 h treatment of MDA-MB-231 cells with CDM resulted in the downregulation of mRNA for cytochrome C oxidase subunits (COX1S, COX4I1, COX5A, COX5B, COX7C) and co-chaperone proteins (COX17, SCO2) that deliver copper to the mitochondria.¹³ These microscopy images cannot prove if the CDM is simply interacting with the copper center in cytochrome C oxidase or if it is sequestering the copper away from the enzyme to prevent redox cycling. Still, the damage of a copper chelator concentrated in mitochondria paves the way for a therapeutic modality, especially in TNBC cell lines.

What causes the mitochondrial structure to change, and how is this related to copper depletion and (ultimately) cell death? Mitochondrial fission and fusion are regulated by a family of proteins. Mitochondria are severed by dynamin-related protein 1 (Drp1), while mitochondria are fused by mitofusins 1 and 2 (Mfn1 and 2) at the outer membrane and by OPA1 at the inner membrane. OPA1 is regulated by the mitochondrial membrane potential, as follows. Humans have eight different isoforms of OPA1, including long and short forms (L-OPA1 and S-OPA1). These are present in nearly equimolar forms under basal conditions.⁵⁹ The L form can be cleaved to the S form by the mitochondrial zinc metalloprotease OMA1 (overlapping with the *m*-AAA protease 1) when the mitochondrial membrane potential is low.⁶⁰ OMA1 is normally degraded by proteolysis, but in low membrane potential situations, OMA1 is stabilized and survives long enough to cleave L-OPA1 to S-OPA1. Thus, OPA pools are determined by the bioenergetic parameter $\Delta\Psi_m$ (mitochondrial membrane potential), the mitochondrial membrane potential: lower membrane potential causes a decrease in OPA1 concentrations, suppressing fusion.

Recently, Sesaki et al.⁶¹ found membrane potential flickering (temporary, transient lowering of mitochondria membrane potential⁶²) in hyperfused mitochondria would serve to keep fusion limited by transiently degrading OPA1.⁶³ Copper is required for the transient membrane potential flickering.⁶¹ Two copper-containing mitochondrial enzymes, superoxide dismutase 1 and cytochrome *c* oxidase, regulate flickering: superoxide dismutase 1 (SOD1) suppresses flickering, whereas cytochrome *c* oxidase promotes it. Knockout of the copper import protein SLC25A3 (Solute Carrier Family 25 Member 3)⁶⁴ resulted in the loss of copper in the mitochondrial matrix, and thus COX activity. In the absence of flickering, OPA1 is not degraded, and so the balance is toward fusion under metabolic stress conditions (e.g., “due to the genetic loss of Drp1 or its receptor or due to metabolic stress caused by depleting methionine and choline in mice”⁶⁰). We postulate that, in our experiments, the CDM in the matrix chelates and thus depletes the bioavailable copper concentration in the matrix, which would result in suppression of transient

flickering, leading to hyperfused and spherical mitochondria, which is exactly what we observe. This model is shown schematically in Figure 7.

The fission/fusion balance in mitochondria involves both the inner and outer membranes. Due to technology limitations, most studies to date only characterize the outer membrane shape, with the inner membrane cristae being beyond the spatial resolution limits of conventional confocal microscopy. TEM imaging by Sesaki et al. found a lack of Cu in the mitochondrial matrix due to the knockout of SLC25A3 protein caused the inner cristae structures to go away,⁶¹ even in cases where the outer ultrastructure was not changed to a spherical morphology. This is similar to what we observed in our experiments with copper chelators. Our work demonstrates that super-resolution imaging of live cells has an important role to play in future studies of mitochondria ultrastructure in electrophysiology at the microscopic level and cancer and the organism level. Put simply, there is an entire unexplored frontier of the internal cristae structure and its role in disease and health, made possible by recent advances in live-cell imaging using super-resolution microscopy.

CONCLUSIONS

In this work, we have shown that the drug delivery mechanism within the cell involves the dissociation of small-molecule CDM from the CDN nanoparticle in the cytoplasm, followed by localization of the CDM in the cristae of the mitochondria. This work shows that the localization of the small-molecule CDM is dependent on the membrane potential of the mitochondria, demonstrating its “drug targeting” mechanism is due to the charged nature of CDM and the mitochondrial electric fields. The mechanism of cytotoxic action involves irreversible structural change (which we interpret as “damage”) to mitochondrial morphology, including fragmentation of the filamentous network into spherical mitochondria and internal cristae remodeling. This is the first (in time) observable cytotoxic effect of copper chelation, which is followed downstream by reduced energy production and respiration and ultimately by cell death. We have proven this is due to the copper chelation, and not some alternative mechanism of the CDM, by (1) control studies with abundant exogenous copper which prevents cytotoxic mitochondria morphology change and (2) careful comparison to other copper chelation pharmacological agents to confirm the mechanism. We have presented a plausible model of the microscopic mechanism based on membrane potential flickering recently observed by others⁶¹ and its relationship to copper in mitochondrial electron transport chain enzyme complexes.

METHODS

Statistical Analysis

To calculate the voltage-dependent manner of CDM-labeling mitochondria, the mean CDM fluorescence intensity of individual cells was recorded before and after the cells were treated with 10 μ M FCCP, and a paired *t*-test was conducted to compare the mean fluorescence intensity of CDM in cells before and after treatment with FCCP. The *p*-value was less than 0.05, indicating that the observed difference in mean fluorescence intensity before and after treatment with FCCP is statistically significant. To calculate cell viability, raw absorbance values were divided by medium-treated wells to obtain normalized absorbance. Triplicate inputs as normalized absorbance were analyzed by nonlinear four-parameter variable slope regression on GraphPad Prism 10.2.2. Standard errors are reported by the

regression function. Cell viabilities are reported as the inhibitory concentration at 50%, and corresponding errors are the standard error of the means.

Cell Culture

MDA-MB-231 cells used in this research were purchased from ATCC. All the cells were cultured for 2–3 days in 75 cm² tissue flasks at 37 °C and 5% CO₂ before experimentation.

CDM and CDN Synthesis and Characterization

CDM was synthesized according to the published procedure.¹⁵ Briefly, IR780 (32.5 mg, 0.051 mmol), *N*¹,*N*¹-bis(pyridine-2-ylmethyl)ethane-1,2-diamine (37 mg, 0.15 mmol), and anhydrous K₂CO₃ (7 mg, 51 μmol) were dissolved in anhydrous DMF. The solution was heated to 80 °C and stirred for 5 h. The solvent was removed, and the mixture was washed with water and brine three times. The crude product was extracted with dichloromethane and purified by silica column chromatography (17 mg). CDN was formulated with a nanoemulsion method. Briefly, 1 mL tetrahydrofuran (THF) solution of semiconducting polymer (Supporting Information Figure S1) (0.125 mg), DPPE-PEG2000 (2.5 mg), and CDM (2.5 μg) was rapidly injected into distilled deionized water (9 mL) under continuous sonication for 2 min. THF was removed, and the aqueous solution was filtered through a 0.22 μm filter. Then, the solution was washed with HEPES buffer and centrifuged to afford the final CDM solution. The size in diameter and zeta potential were measured to be 93 nm and 6.69 mV, respectively, by dynamic light scattering (Malvern ZetaSizer Nano S).

Live Cell Fluorescent Microscopy of Mitochondrial Dynamics

Cells were seeded in CELLview four-compartment glass-bottom tissue culture dishes (Greiner Bio-Ones, 627870), PS, 35/10 mm, 24 h before imaging. The live cell experiments were performed in the Zeiss LSM900 microscope under ambient condition. Imaging of cells was performed using an Airyscan alpha Plan-Apochromat 63×/1.4 Oil DIC M27 objective. Laser lines of 488, 561, and 641 nm were used. The laser powers were adjusted between approximately 0.3% and 2%, and the master gain was between 750 and 900. We started continuous scanning at a maximum speed at a zoom factor of 1, in order to obtain a relatively strong signal-to-noise ratio for imaging. Later, we brought the field of mitochondria of interest into view and stopped scanning. The pixel dwell time was set between 0.85 and 1.04 μs, respectively, to avoid overtime exposure of mitochondria to the laser. MTG (excitation at 488 nm, emission at 450–561 nm) was used for structural imaging, and TMRE (excitation at 561 nm, emission at 561–700 nm) was used for voltage imaging. CDM was observed at 642–700 nm (excitation at 641 nm).

Mitochondrial Morphology Rescued by Copper Addition

Additional copper ions were added after CDM incubation to verify the rescue effects for the mitochondrial morphology. The MDA-MB-231 cells were seeded into the test and control groups. Both groups were first incubated with 1 μM CDM for 30 min, then washed with phosphate-buffered saline (PBS) 3 times to remove excessive CDM. Later, the MDA-MB-231 cells were incubated with Hanks' balanced salt solution (HBSS) buffer for 30 min to eliminate the chance of copper binding to substances such as GSH, BSA, and various amino acids. The MDA-MB-231 cells were then washed again with PBS 3 times and incubated with Roswell Park Memorial Institute (RPMI) medium for long-term observation. Once the dish was set up on the microscope, 10 μM copper ions were added to the test group and imaging was started at 0.5, 1, and 2 h to compare mitochondrial morphology with the control group.

Cell Viability of MDA-MB-231 Cells with CDM, IR780, and ATN-224 Treatments

To a 96-well plate, 10,000 cells were seeded per well, in triplicate per treatment condition. Cells were first counted by the Trypan Blue exclusion method and then diluted into DMEM supplemented with 10% fetal bovine serum (FBS) and 1% penicillin/streptomycin. Cells

were cultured at 37 °C with 5% CO₂ atmosphere. The compounds were prepared in a 10 mM solution in dimethyl sulfoxide (DMSO), ensuring full solubility by gentle heating up to 37 °C. Then, the DMSO solution was serially diluted in the media to obtain concentrations ranging from 100 nM to 100 μM. A no-treatment, media-only condition was used to normalize the cell viability data.

After being seeded, the cells were incubated at 37 °C overnight so that they would adhere to the bottom of the well. The next morning, the old medium was removed from the wells, and the fresh medium containing the compounds was added to the cells in 100 μL. Each compound and concentration had at least three triplicates. The cells were incubated at 37 °C for 24 h with the compound. The next day, the medium containing the compounds was removed. Then, 100 μL of media containing 10% of MTT reagent (Sigma-Aldrich cat. no. M5655) was added to each well. The plate was allowed to develop formazan at 37 °C in the dark for over 3 h, and then the absorbance at 590 nm was read from each well. IC₅₀ values were obtained from GraphPad Prism version 10.2.2. Graph was generated in Microsoft Excel.

Sphericity Calculations

We used an algorithm called “mitoAnnotation” to calculate the sphericity of mitochondria, which is publicly available (<https://github.com/shiown026/mitoAnnotation>). We have previously explained this method in the previous study.²¹ Sphericity is a unitless number calculated using the formula: $\text{sphericity} = 4\pi \times (\text{area}/\text{perimeter}^2)$ where a value of 1.0 indicates a perfect circle. As the value approaches 0.0, it means an increasingly elongated polygon (tubular).⁶⁵

Source fluorescence images were first subjected to background subtraction to ensure accurate mitochondrial segmentation using a rolling ball algorithm. Then, Otsu's method⁶⁶ was applied to determine the optimal intensity threshold for binarization, effectively separating mitochondrial signal from background fluorescence.⁶⁷ The resulting binary masks were further processed by using morphological operations (e.g., hole filling and edge smoothing) to isolate individual mitochondrial structures. After that, we replaced each isolated mitochondrion on the original image and manually inspected it to ensure that it was isolated correctly, especially in areas where the image was crowded or had low contrast. The area and perimeter of each mitochondrion were measured, and the sphericity value was calculated accordingly. In some data sets, to make the image more transparent and reduce background variability, we also used other methods, such as K-means and top-hat filtering, which have been previously proposed in previous studies.⁶⁸

This method helps us to measure the shape of mitochondria accurately and reproducibly under different experimental conditions. Additional quantitative data, including individual area, perimeter, and sphericity values for each sample, are given in Table S1. Corresponding binary mask and detected contour images are shown in Figures S10 and S12, and box plot visualizations of sphericity distributions are displayed under each condition (S13–S15).

Image Analysis and Quantification

We used binarized images to obtain mitochondrial length, width, and branching count and performed these measurements with ImageJ software. The Mann–Whitney *U* test was used in GraphPad Prism version 10.2.2 for statistical comparisons between the groups. Full details of the analysis steps are provided in the Supporting Information.

■ ASSOCIATED CONTENT

Supporting Information

The Supporting Information is available free of charge at <https://pubs.acs.org/doi/10.1021/jacsau.5c00035>.

Chemical structures of all compounds; additional fluorescence microscopy images of cells incubated with CDM, IR780, ATN-224, or TMRE; details of image analysis and quantification, sphericity calculation, and

illumination energy doses; statistical analysis; and kinetics of CDM release from CDN (PDF)

AUTHOR INFORMATION

Corresponding Authors

Peter J. Burke – Department of Biomedical Engineering, University of California, Irvine, California 92697, United States; Department of Electrical Engineering and Computer Science, University of California, Irvine, California 92697, United States; orcid.org/0000-0002-8883-1014; Email: pburke@uci.edu

Jianghong Rao – Department of Radiology, Molecular Imaging Program at Stanford, Stanford University School of Medicine, Stanford, California 94305, United States; orcid.org/0000-0002-5143-9529; Email: jrao@stanford.edu

Authors

ChiaHung Lee – Department of Biomedical Engineering, University of California, Irvine, California 92697, United States

Zhen Xiao – Department of Radiology, Molecular Imaging Program at Stanford, Stanford University School of Medicine, Stanford, California 94305, United States

Irene Lim – Department of Radiology, Molecular Imaging Program at Stanford, Stanford University School of Medicine, Stanford, California 94305, United States; Present Address: Department of Chemistry and Biochemistry, Bates College, Lewiston, Maine 04240, United States

Ting Wang – Department of Radiology, Molecular Imaging Program at Stanford, Stanford University School of Medicine, Stanford, California 94305, United States

Parisa Aghaei – Department of Electrical Engineering and Computer Science, University of California, Irvine, California 92697, United States

Complete contact information is available at: <https://pubs.acs.org/10.1021/jacsau.5c00035>

Author Contributions

The manuscript was written through the contributions of all authors. All authors have approved the final version of the manuscript.

Notes

The authors declare no competing financial interest. Any additional relevant notes should be placed here.

ACKNOWLEDGMENTS

This work was supported in part by NIH grant 1R01CA259635-01A1 and 3R01CA243033-03S1A1, the National Science Foundation (NSF) award #2153425, and the Army Research Office through the ARO (contract nos. W911NF-18-1-0076, W911NF-19-10369, and W911NF-20-10103) and the AFOSR. I.L. acknowledges the support of the NCI-funded Stanford Molecular Imaging Scholar (SMIS) Training grant (T32CA118681). This material is based upon work supported by the Air Force Office of Scientific Research under award numbers FA9550-23-1-0436 and FA9550-23-1-0061. Any opinions, findings, conclusions, or recommendations expressed in this material are those of the author(s) and do not necessarily reflect the views of the United States Air Force.

ABBREVIATIONS

ATP, adenosine triphosphate; FCCP, carbonyl cyanide-*p*-trifluoromethoxy phenylhydrazone; CDM, copper-chelating moiety; CDN, copper-depleting nanoparticles; Cu, copper; CytC, cytochrome C; MTG, MitoTracker Green; MTT, 3-(4,5-dimethylthiazol-2-yl)-2,5-diphenyltetrazolium bromide; OPA1, optic atrophy protein 1; SIM, structured illumination microscopy; STED, stimulated emission depletion; TEM, transmission electron microscopy; TMRE, tetramethyl rhodamine ethyl ester; TNBC, triple negative breast cancer; TTM, tetrathiomolybdate; PBS, phosphate-buffered saline; HBSS, Hanks' balanced salt solution; DMSO, dimethyl sulfoxide; RPMI, Roswell Park Memorial Institute; FBS, fetal bovine serum; COX, cytochrome C oxidase; IC₅₀, inhibitory concentration at 50%; $\Delta\Psi_m$, mitochondrial membrane potential; OMA1, overlapping with the *m*-AAA protease 1; SLC25A3, solute carrier family 25 member 3; SOD1, superoxide dismutase 1

REFERENCES

- (1) Tsang, T.; Davis, C. I.; Brady, D. C. Copper Biology. *Curr. Biol.* **2021**, *31* (9), R421–R427.
- (2) Ruiz, L. M.; Libedinsky, A.; Elorza, A. A. Role of Copper on Mitochondrial Function and Metabolism. *Front. Mol. Biosci.* **2021**, *8*, 1–17.
- (3) Solier, S.; Müller, S.; Cañeque, T.; Versini, A.; Mansart, A.; Sindikubwabo, F.; Baron, L.; Emam, L.; Gestraud, P.; Pantoş, G. D.; Gandon, V.; Gaillet, C.; Wu, T. D.; Dingli, F.; Loew, D.; Baulande, S.; Durand, S.; Sencio, V.; Robil, C.; Trottein, F.; Péricat, D.; Näser, E.; Cougoule, C.; Meunier, E.; Bègue, A. L.; Salmon, H.; Manel, N.; Puisieux, A.; Watson, S.; Dawson, M. A.; Servant, N.; Kroemer, G.; Annane, D.; Rodriguez, R. A Druggable Copper-Signaling Pathway That Drives Inflammation. *Nature* **2023**, *617* (7960), 386–394.
- (4) Kaplan, J. H.; Maryon, E. B. How Mammalian Cells Acquire Copper: An Essential but Potentially Toxic Metal. *Biophys. J.* **2016**, *110* (1), 7–13.
- (5) Cobine, P. A.; Pierrel, F.; Winge, D. R. Copper Trafficking to the Mitochondrion and Assembly of Copper Metalloenzymes. *Biochim. Biophys. Acta, Mol. Cell Res.* **2006**, *1763* (7), 759–772.
- (6) Pham, V. N.; Chang, C. J. Metalloallostery and Transition Metal Signaling: Bioinorganic Copper Chemistry Beyond Active Sites. *Angew. Chem., Int. Ed.* **2023**, *62* (11), No. e202213644.
- (7) Shanbhag, V. C.; Gudekar, N.; Jasmer, K.; Papageorgiou, C.; Singh, K.; Petris, M. J. Copper Metabolism as a Unique Vulnerability in Cancer. *Biochim. Biophys. Acta, Mol. Cell Res.* **2021**, *1868* (2), 118893.
- (8) Li, Y. Copper Homeostasis: Emerging Target for Cancer Treatment. *IUBMB Life* **2020**, *72* (9), 1900–1908.
- (9) Li, S.-R.; Bu, L.-L.; Cai, L. Cuproptosis: Lipoylated TCA Cycle Proteins-Mediated Novel Cell Death Pathway. *Signal Transduct. Targeted Ther.* **2022**, *7* (1), 158.
- (10) Aubert, L.; Nandagopal, N.; Steinhart, Z.; Lavoie, G.; Nourreddine, S.; Berman, J.; Saba-El-Leil, M. K.; Papadopoulos, D.; Lin, S.; Hart, T.; Macleod, G.; Topisirovic, I.; Gaboury, L.; Fahmi, C. J.; Schramek, D.; Meloche, S.; Angers, S.; Roux, P. P. Copper Bioavailability Is a KRAS-Specific Vulnerability in Colorectal Cancer. *Nat. Commun.* **2020**, *11* (1), 3701.
- (11) Blockhuys, S.; Celauro, E.; Hildesjö, C.; Feizi, A.; Stål, O.; Fierro-González, J. C.; Wittung-Stafshede, P. Defining the Human Copper Proteome and Analysis of Its Expression Variation in Cancers. *Metallomics* **2017**, *9* (2), 112–123.
- (12) Ge, E. J.; Bush, A. I.; Casini, A.; Cobine, P. A.; Cross, J. R.; DeNicola, G. M.; Dou, Q. P.; Franz, K. J.; Gohil, V. M.; Gupta, S.; Kaler, S. G.; Lutsenko, S.; Mittal, V.; Petris, M. J.; Polishchuk, R.; Ralle, M.; Schilsky, M. L.; Tonks, N. K.; Vahdat, L. T.; Van Aelst, L.; Xi, D.; Yuan, P.; Brady, D. C.; Chang, C. J. Connecting Copper and

- Cancer: From Transition Metal Signalling to Metalloplasia. *Nat. Rev. Cancer* **2022**, *22* (2), 102–113.
- (13) Chan, N.; Willis, A.; Kornhauser, N.; Ward, M. M.; Lee, S. B.; Nackos, E.; Seo, B. R.; Chuang, E.; Cigler, T.; Moore, A.; Donovan, D.; Vallee Cobham, M.; Fitzpatrick, V.; Schneider, S.; Wiener, A.; Guillaume-Abraham, J.; Aljom, E.; Zelkowitz, R.; Warren, J. D.; Lane, M. E.; Fischbach, C.; Mittal, V.; Vahdat, L. Influencing the Tumor Microenvironment: A Phase II Study of Copper Depletion Using Tetrathiomolybdate in Patients with Breast Cancer at High Risk for Recurrence and in Preclinical Models of Lung Metastases. *Clin. Cancer Res.* **2017**, *23* (3), 666–676.
- (14) Blockhuys, S.; Hildesjö, C.; Olsson, H.; Vahdat, L.; Wittung-Stafshede, P. Evaluation of ATOX1 as a Potential Predictive Biomarker for Tetrathiomolybdate Treatment of Breast Cancer Patients with High Risk of Recurrence. *Biomedicines* **2021**, *9* (12), 1887.
- (15) Cui, L.; Gouw, A. M.; LaGory, E. L.; Guo, S.; Attarwala, N.; Tang, Y.; Qi, J.; Chen, Y.-S.; Gao, Z.; Casey, K. M.; Bazhin, A. A.; Chen, M.; Hu, L.; Xie, J.; Fang, M.; Zhang, C.; Zhu, Q.; Wang, Z.; Giaccia, A. J.; Gambhir, S. S.; Zhu, W.; Felsher, D. W.; Pegram, M. D.; Goun, E. A.; Le, A.; Rao, J. Mitochondrial Copper Depletion Suppresses Triple-Negative Breast Cancer in Mice. *Nat. Biotechnol.* **2021**, *39* (3), 357–367.
- (16) Jeena, M. T.; Kim, S.; Jin, S.; Ryu, J.-H. Recent Progress in Mitochondria-Targeted Drug and Drug-Free Agents for Cancer Therapy. *Cancers* **2020**, *12* (1), 4.
- (17) Ramchandani, D.; Berisa, M.; Tavarez, D. A.; Li, Z.; Miele, M.; Bai, Y.; Lee, S. B.; Ban, Y.; Dephoure, N.; Hendrickson, R. C.; Cloonan, S. M.; Gao, D.; Cross, J. R.; Vahdat, L. T.; Mittal, V. Copper Depletion Modulates Mitochondrial Oxidative Phosphorylation to Impair Triple Negative Breast Cancer Metastasis. *Nat. Commun.* **2021**, *12* (1), 7311.
- (18) Zhou, P.; Qin, J.; Zhou, C.; Wan, G.; Liu, Y.; Zhang, M.; Yang, X.; Zhang, N.; Wang, Y. Multifunctional Nanoparticles Based on a Polymeric Copper Chelator for Combination Treatment of Metastatic Breast Cancer. *Biomaterials* **2019**, *195*, 86–99.
- (19) Lee, C.; Wallace, D. C.; Burke, P. J. Super-Resolution Imaging of Voltages in the Interior of Individual, Vital Mitochondria. *ACS Nano* **2024**, *18* (2), 1345–1356.
- (20) Chazotte, B. Labeling Mitochondria with MitoTracker Dyes. *Cold Spring Harb. Protoc.* **2011**, *2011* (8), pdb.prot5648.
- (21) Lee, C.-H.; Wallace, D. C.; Burke, P. J. Photobleaching and Phototoxicity of Mitochondria in Live Cell Fluorescent Super-Resolution Microscopy. *Mitochondrial Commun.* **2024**, *2* (March), 38–47.
- (22) Klein Geltink, R. I.; O'Sullivan, D.; Corrado, M.; Bremser, A.; Buck, M. D.; Buescher, J. M.; Firat, E.; Zhu, X.; Niedermann, G.; Caputa, G.; Kelly, B.; Warthorst, U.; Rensing-Ehl, A.; Kyle, R. L.; Vandersarren, L.; Curtis, J. D.; Patterson, A. E.; Lawless, S.; Grzes, K.; Qiu, J.; Sanin, D. E.; Kretz, O.; Huber, T. B.; Janssens, S.; Lambrecht, B. N.; Rambold, A. S.; Pearce, E. J.; Pearce, E. L. Mitochondrial Priming by CD28. *Cell* **2017**, *171* (2), 385–397.
- (23) Rasmussen, M. L.; Taneja, N.; Neining, A. C.; Wang, L.; Robertson, G. L.; Riffle, S. N.; Shi, L.; Knollmann, B. C.; Burnette, D. T.; Gama, V. MCL-1 Inhibition by Selective BH3Mimetics Disrupts Mitochondrial Dynamics Causing Loss of Viability and Functionality of Human Cardiomyocytes. *iScience* **2020**, *23* (4), 101015.
- (24) Bahat, A.; Goldman, A.; Zaltsman, Y.; Khan, D. H.; Halperin, C.; Amzallag, E.; Krupalnik, V.; Mullokanov, M.; Silberman, A.; Erez, A.; Schimmer, A. D.; Hanna, J. H.; Gross, A. MTCH2-Mediated Mitochondrial Fusion Drives Exit from Naïve Pluripotency in Embryonic Stem Cells. *Nat. Commun.* **2018**, *9* (1), 5132.
- (25) Bagamery, L. E.; Justman, Q. A.; Garner, E. C.; Murray, A. W. A Putative Bet-Hedging Strategy Buffers Budding Yeast against Environmental Instability. *Curr. Biol.* **2020**, *30* (23), 4563–4578.
- (26) Cackovic, J.; Gutierrez-Luke, S.; Call, G. B.; Juba, A.; O'Brien, S.; Jun, C. H.; Buhlman, L. M. Vulnerable Parkin Loss-of-Function Drosophila Dopaminergic Neurons Have Advanced Mitochondrial Aging, Mitochondrial Network Loss and Transiently Reduced Autophagosome Recruitment. *Front. Cell. Neurosci.* **2018**, *12* (February), 39.
- (27) Balboa, E.; Castro, J.; Pinochet, M.-J.; Cancino, G. I.; Matias, N.; Sáez, P. J.; Martínez, A.; Álvarez, A. R.; García-Ruiz, C.; Fernández-Checa, J. C.; Zanlungo, S. MLN64 Induces Mitochondrial Dysfunction Associated with Increased Mitochondrial Cholesterol Content. *Redox Biol.* **2017**, *12* (March), 274–284.
- (28) Lin, Y.-T.; Lin, K.-H.; Huang, C.-J.; Wei, A.-C. MitoTox: A Comprehensive Mitochondrial Toxicity Database. *BMC Bioinf.* **2021**, *22* (S10), 369.
- (29) Ritchie, R. J. A Critical Assessment of the Use of Lipophilic Cations as Membrane Potential Probes. *Prog. Biophys. Mol. Biol.* **1984**, *43* (1), 1–32.
- (30) Severina, F. F.; Severina, I. I.; Antonenko, Y. N.; Rokitskaya, T. I.; Cherepanov, D. A.; Mokhova, E. N.; Vysokikh, M. Y.; Pustovidko, A. V.; Markova, O. V.; Yaguzhinsky, L. S.; et al. Penetrating Cation/Fatty Acid Anion Pair as a Mitochondria-Targeted Protonophore. *Proc. Natl. Acad. Sci. U.S.A.* **2010**, *107* (2), 663–668.
- (31) Scaduto, R. C.; Grotyohann, L. W. Measurement of Mitochondrial Membrane Potential Using Fluorescent Rhodamine Derivatives. *Biophys. J.* **1999**, *76* (1), 469–477.
- (32) Trnka, J.; Elkalaf, M.; Anděl, M. Lipophilic Triphenylphosphonium Cations Inhibit Mitochondrial Electron Transport Chain and Induce Mitochondrial Proton Leak. *PLoS One* **2015**, *10* (4), No. e0121837.
- (33) Minamikawa, T.; Sriratana, A.; Williams, D. A.; Bowser, D. N.; Hill, J. S.; Nagley, P. Chloromethyl-X-Rosamine (MitoTracker Red) Photosensitizes Mitochondria and Induces Apoptosis in Intact Human Cells. *J. Cell Sci.* **1999**, *112* (14), 2419–2430.
- (34) Hackenbrock, C. R. Ultrastructural Bases For Metabolically Linked Mechanical Activity In Mitochondria: I. Reversible Ultrastructural Changes with Change in Metabolic Steady State in Isolated Liver Mitochondria. *J. Cell Biol.* **1966**, *30* (2), 269–297.
- (35) Hackenbrock, C. R. Ultrastructural Bases For Metabolically Linked Mechanical Activity In Mitochondria: II. Electron Transport-Linked Ultrastructural Transformations in Mitochondria. *J. Cell Biol.* **1968**, *37* (2), 345–369.
- (36) Cogliati, S.; Frezza, C.; Soriano, M. E.; Varanita, T.; Quintana-Cabrera, R.; Corrado, M.; Cipolat, S.; Costa, V.; Casarin, A.; Gomes, L. C.; Perales-Clemente, E.; Salvati, L.; Fernandez-Silva, P.; Enriquez, J. A.; Scorrano, L. Mitochondrial Cristae Shape Determines Respiratory Chain Supercomplexes Assembly and Respiratory Efficiency. *Cell* **2013**, *155* (1), 160–171.
- (37) Patten, D. A.; Wong, J.; Khacho, M.; Soubannier, V.; Mailloux, R. J.; Pilon-Larose, K.; MacLaurin, J. G.; Park, D. S.; McBride, H. M.; Trinkle-Mulcahy, L.; Harper, M.; Germain, M.; Slack, R. S. OPA1-dependent Cristae Modulation Is Essential for Cellular Adaptation to Metabolic Demand. *EMBO J.* **2014**, *33* (22), 2676–2691.
- (38) Glancy, B.; Kim, Y.; Katti, P.; Willingham, T. B. The Functional Impact of Mitochondrial Structure Across Subcellular Scales. *Front. Physiol.* **2020**, *11* (November), 1–24.
- (39) Anand, R.; Reichert, A. S.; Kondadi, A. K. Emerging Roles of the MICOS Complex in Cristae Dynamics and Biogenesis. *Biology* **2021**, *10* (7), 600.
- (40) Kondadi, A. K.; Anand, R.; Reichert, A. S. Cristae Membrane Dynamics – A Paradigm Change. *Trends Cell Biol.* **2020**, *30* (12), 923–936.
- (41) Iovine, J. C.; Claypool, S. M.; Alder, N. N. Mitochondrial Compartmentalization: Emerging Themes in Structure and Function. *Trends Biochem. Sci.* **2021**, *46* (11), 902–917.
- (42) Glancy, B. Visualizing Mitochondrial Form and Function within the Cell. *Trends Mol. Med.* **2020**, *26* (1), 58–70.
- (43) Wang, C.; Taki, M.; Sato, Y.; Tamura, Y.; Yaginuma, H.; Okada, Y.; Yamaguchi, S. A Photostable Fluorescent Marker for the Superresolution Live Imaging of the Dynamic Structure of the Mitochondrial Cristae. *Proc. Natl. Acad. Sci. U.S.A.* **2019**, *116* (32), 15817–15822.
- (44) Liu, T.; Stephan, T.; Chen, P.; Keller-Findeisen, J.; Chen, J.; Riedel, D.; Yang, Z.; Jakobs, S.; Chen, Z. Multi-Color Live-Cell STED

Nanoscopy of Mitochondria with a Gentle Inner Membrane Stain. *Proc. Natl. Acad. Sci. U.S.A.* **2022**, *119* (52), 2017.

(45) Rogers, G. W.; Brand, M. D.; Petrosyan, S.; Ashok, D.; Elorza, A. A.; Ferrick, D. A.; Murphy, A. N. High Throughput Microplate Respiratory Measurements Using Minimal Quantities Of Isolated Mitochondria. *PLoS One* **2011**, *6* (7), No. e21746.

(46) Colasuonno, F.; Borghi, R.; Niceforo, A.; Muzzi, M.; Bertini, E.; Di Giulio, A.; Moreno, S.; Compagnucci, C. Senescence-Associated Ultrastructural Features of Long-Term Cultures of Induced Pluripotent Stem Cells (iPSCs). *Aging* **2017**, *9* (10), 2209–2222.

(47) Buck, M. D.; O'Sullivan, D.; Klein Geltink, R. I.; Curtis, J. D.; Chang, C.-H.; Sanin, D. E.; Qiu, J.; Kretz, O.; Braas, D.; van der Windt, G. J. W.; Chen, Q.; Huang, S. C.-C.; O'Neill, C. M.; Edelson, B. T.; Pearce, E. J.; Sesaki, H.; Huber, T. B.; Rambold, A. S.; Pearce, E. L. Mitochondrial Dynamics Controls T Cell Fate through Metabolic Programming. *Cell* **2016**, *166* (1), 63–76.

(48) Scorrano, L.; Ashiya, M.; Buttle, K.; Weiler, S.; Oakes, S. A.; Mannella, C. A.; Korsmeyer, S. J. A Distinct Pathway Remodels Mitochondrial Cristae and Mobilizes Cytochrome c during Apoptosis. *Dev. Cell* **2002**, *2* (1), 55–67.

(49) Frezza, C.; Cipolat, S.; Martins de Brito, O.; Micaroni, M.; Bezoussenko, G. V.; Rudka, T.; Bartoli, D.; Polishuck, R. S.; Danial, N. N.; De Strooper, B.; Scorrano, L. OPA1 Controls Apoptotic Cristae Remodeling Independently from Mitochondrial Fusion. *Cell* **2006**, *126* (1), 177–189.

(50) Sun, M. G.; Williams, J.; Munoz-Pinedo, C.; Perkins, G. A.; Brown, J. M.; Ellisman, M. H.; Green, D. R.; Frey, T. G. Correlated Three-Dimensional Light and Electron Microscopy Reveals Transformation of Mitochondria during Apoptosis. *Nat. Cell Biol.* **2007**, *9* (9), 1057–1065.

(51) Yamaguchi, R.; Lartigue, L.; Perkins, G.; Scott, R. T.; Dixit, A.; Kushnareva, Y.; Kuwana, T.; Ellisman, M. H.; Newmeyer, D. D. Opa1-Mediated Cristae Opening Is Bax/Bak and BH3 Dependent, Required for Apoptosis, and Independent of Bak Oligomerization. *Mol. Cell* **2008**, *31* (4), 557–569.

(52) Yamaguchi, R.; Perkins, G. Dynamics of Mitochondrial Structure during Apoptosis and the Enigma of Opa1. *Biochim. Biophys. Acta, Bioenerg.* **2009**, *1787* (8), 963–972.

(53) Singh, R.; Letai, A.; Sarosiek, K. Regulation of Apoptosis in Health and Disease: The Balancing Act of BCL-2 Family Proteins. *Nat. Rev. Mol. Cell Biol.* **2019**, *20* (3), 175–193.

(54) Montero, J.; Letai, A. Why Do BCL-2 Inhibitors Work and Where Should We Use Them in the Clinic? *Cell Death Differ.* **2018**, *25* (1), 56–64.

(55) Juárez-Salcedo, L. M.; Desai, V.; Dalia, S. Venetoclax: Evidence to Date and Clinical Potential. *Drugs Context* **2019**, *8*, 1–13.

(56) McArthur, K.; Whitehead, L. W.; Heddleston, J. M.; Li, L.; Padman, B. S.; Oorschot, V.; Geoghegan, N. D.; Chappaz, S.; Davidson, S.; San Chin, H.; Lane, R. M.; Dramicanin, M.; Saunders, T. L.; Sugiana, C.; Lessene, R.; Osellame, L. D.; Chew, T.-L.; Dewson, G.; Lazarou, M.; Ramm, G.; Lessene, G.; Ryan, M. T.; Rogers, K. L.; van Delft, M. F.; Kile, B. T. BAK/BAX Macropores Facilitate Mitochondrial Herniation and MtDNA Efflux during Apoptosis. *Science* **2018**, *359* (6378), No. eaao6047.

(57) Pham, T. D.; Pham, P. Q.; Li, J.; Letai, A. G.; Wallace, D. C.; Burke, P. J. Cristae Remodeling Causes Acidification Detected by Integrated Graphene Sensor during Mitochondrial Outer Membrane Permeabilization. *Sci. Rep.* **2016**, *6* (1), 35907.

(58) Burke, P. J. Mitochondria, Bioenergetics and Apoptosis in Cancer. *Trends Cancer* **2017**, *3* (12), 857–870.

(59) MacVicar, T.; Langer, T. OPA1 Processing in Cell Death and Disease—The Long and Short of It. *J. Cell Sci.* **2016**, *129* (12), 2297–2306.

(60) Head, B.; Griparic, L.; Amiri, M.; Gandre-Babbe, S.; van der Bliek, A. M. Inducible Proteolytic Inactivation of OPA1 Mediated by the OMA1 Protease in Mammalian Cells. *J. Cell Biol.* **2009**, *187* (7), 959–966.

(61) Murata, D.; Roy, S.; Lutsenko, S.; Iijima, M.; Sesaki, H. Slc25a3-Dependent Copper Transport Controls Flickering-Induced

Opa1 Processing for Mitochondrial Safeguard. *Dev. Cell* **2024**, *59* (19), 2578–2592.

(62) Burke, P. J. Mitochondria, Bioenergetics and Apoptosis in Cancer. *Trends Cancer* **2017**, *3* (12), 857–870.

(63) Murata, D.; Yamada, T.; Tokuyama, T.; Arai, K.; Quirós, P. M.; López-Otín, C.; Iijima, M.; Sesaki, H. Mitochondrial Safeguard: A Stress Response That Offsets Extreme Fusion and Protects Respiratory Function via Flickering-Induced OMA1 Activation. *EMBO J.* **2020**, *39* (24), No. e105074.

(64) Boulet, A.; Vest, K. E.; Maynard, M. K.; Gammon, M. G.; Russell, A. C.; Mathews, A. T.; Cole, S. E.; Zhu, X.; Phillips, C. B.; Kwong, J. Q.; Dodani, S. C.; Leary, S. C.; Cobine, P. A. The Mammalian Phosphate Carrier SLC25A3 Is a Mitochondrial Copper Transporter Required for Cytochrome c Oxidase Biogenesis. *J. Biol. Chem.* **2018**, *293* (6), 1887–1896.

(65) Schneider, C. A.; Rasband, W. S.; Eliceiri, K. W. NIH Image to ImageJ: 25 years of image analysis. *Nat. Methods* **2012**, *9* (7), 671–675.

(66) Otsu, N. A Threshold Selection Method from Gray-Level Histograms. *IEEE Trans. Syst., Man, Cybern.* **1979**, *9* (1), 62–66.

(67) Valente, A. J.; Maddalena, L. A.; Robb, E. L.; Moradi, F.; Stuart, J. A. A Simple ImageJ Macro Tool for Analyzing Mitochondrial Network Morphology in Mammalian Cell Culture. *Acta Histochem.* **2017**, *119* (3), 315–326.

(68) Sternberg, S. R. Biomedical Image Processing. *IEEE Comput.* **1983**, *16* (1), 22–34.

Supplementary Materials for
Copper chelation induces morphology change in mitochondria of triple-negative breast cancer

ChiaHung Lee,¹ Zhen Xiao,² Irene Lim,²† Ting Wang,² Parisa Aghaei,³ Peter J. Burke*,^{1,3}
Jianghong Rao*²

¹ Department of Biomedical Engineering, University of California, Irvine, California 92697, United States.

² Department of Radiology, Molecular Imaging Program at Stanford, Stanford University School of Medicine, Stanford, CA 94305, United States.

³ Department of Electrical Engineering and Computer Science, University of California, Irvine, California 92697, United States

† Department of Chemistry and Biochemistry, Bates College, Lewiston, Maine 04240, United States

This PDF file includes:

Figures S1 to S19

Tables S1 to S5

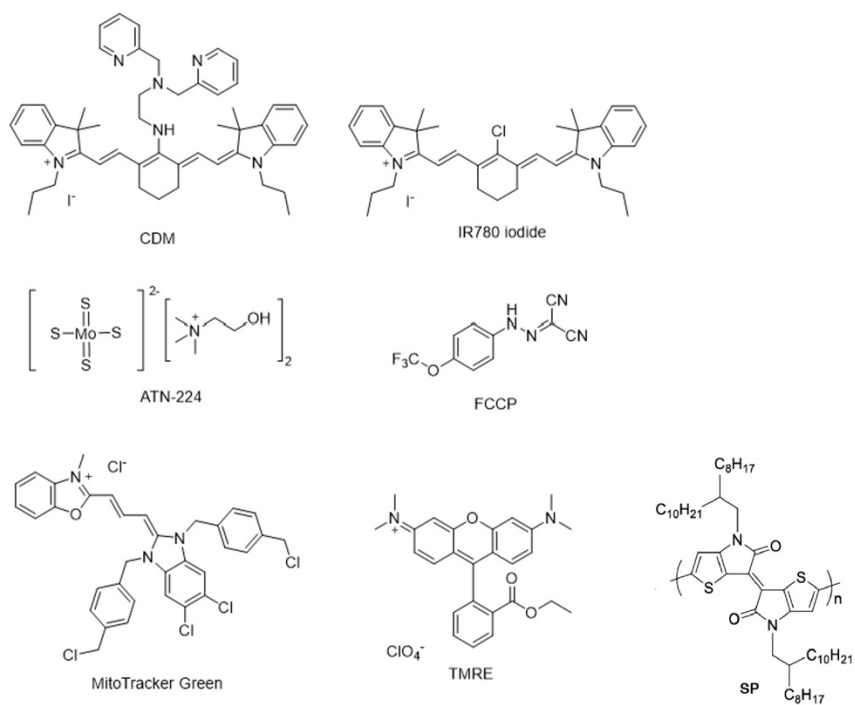


Figure S1. Chemical structures of molecules and nanostructures used in this study, including CDM, IR780 iodide, ATN-224, FCCP, MitoTracker Green, TMRE, and semiconducting polymer (SP) structure.

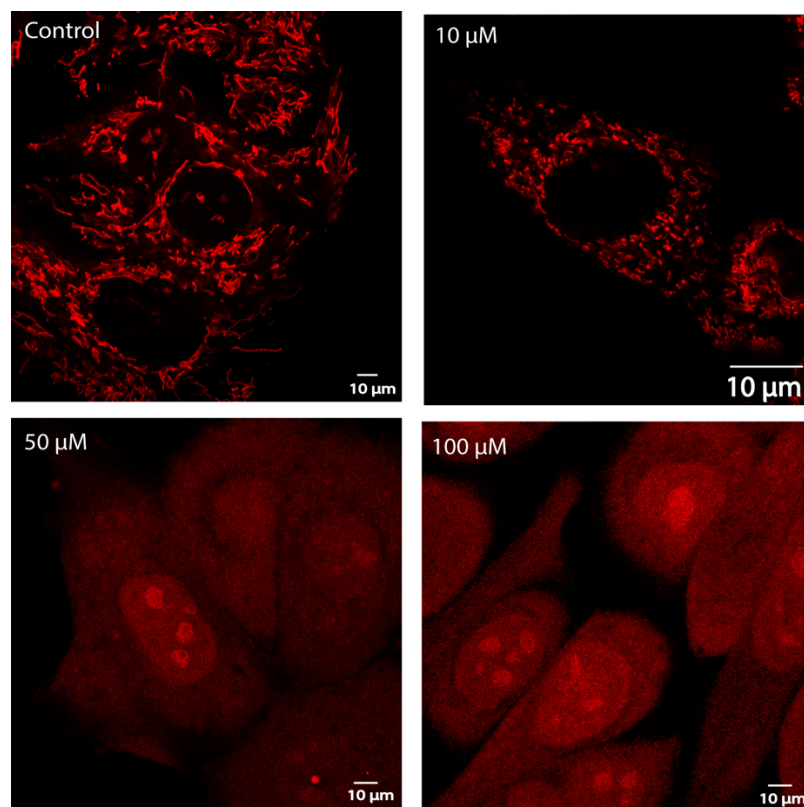


Figure S2. Dose-dependence study of IR780. MBA-MD-231 cells were treated with 10 nM TMRE for 15 min, then with 0, 10 μ M, 50 μ M, or 100 μ M of IR780 for 5 min, then imaged (ex. 561 nm, em. 550-700 nm). Scale bar = 10 μ m.

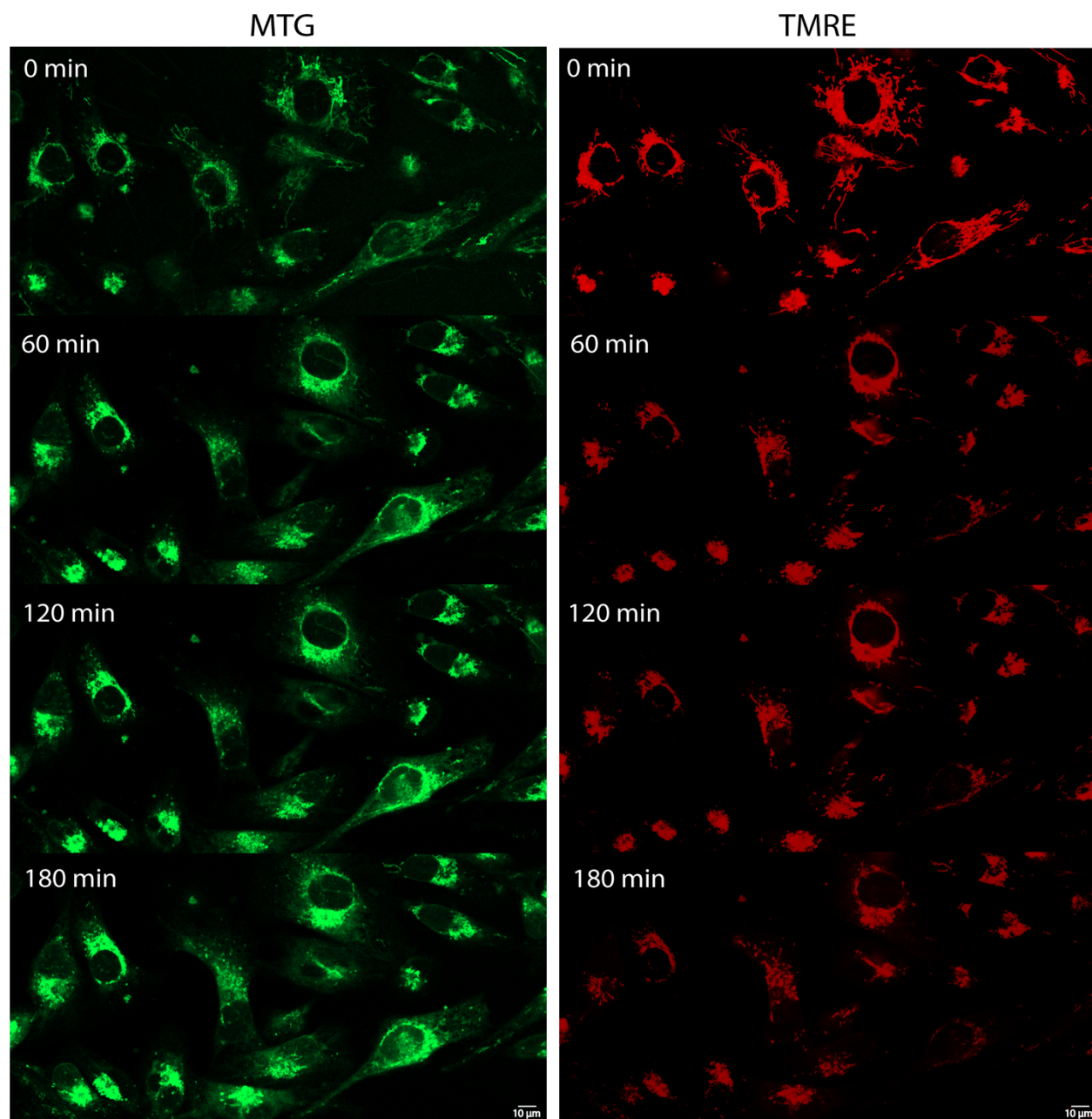


Figure S3. Time course study of ATN-224

MDA-MB-231 cells were treated with 10 nM TMRE and 10 nM of MTG, then treated with 5 μ M ATN-224 for 180 min. The cells were imaged under two channels (MTG, ex. 488 nm; TMRE, ex. 561 nm)

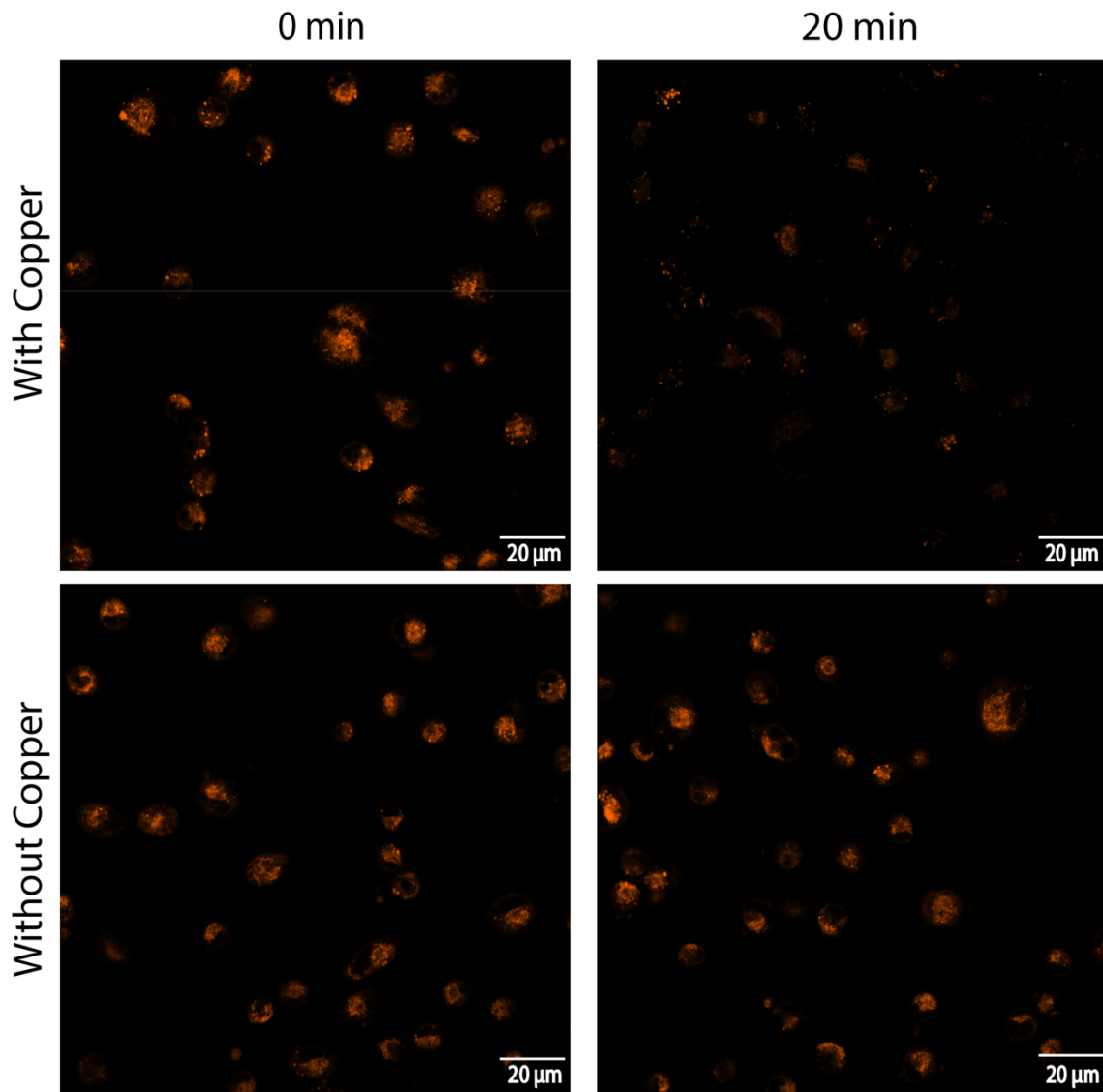


Figure S4. Copper is chelated by CDM in cells in this study. (A) MDA-MB-231 cells were incubated with 1 μM CDM for 30 min, washed with HBSS for 30 min, then treated with media with or without 10 μM CuCl_2 for 20 min. When copper is complexed to CDM, the fluorescence intensity decreases, proving the copper is complexed to CDM in the cells in this experimental situation. Scale bar = 20 μm .

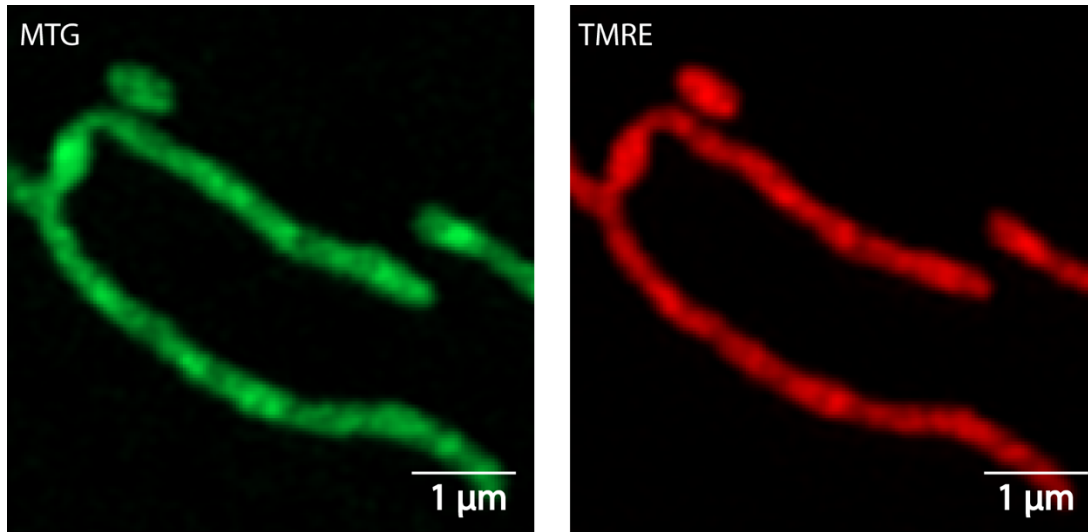


Figure S5. MTG/TMRE overlap. MDA-MB-231 cells cultured for 48 hours with MTG and TMRE staining, demonstrating TMRE and MTG both label the cristae. (Objective x63, pixel size: 43 x 43 nm). Scale bar = 1 μm .

Additional images showing cristae binding of CDM (colocalized with TMRE) are shown in various experiments presented in Fig. S6-S9.

Method for Figs. S6-S9:

1. Stain MB231 cells with 10 nM TMRE and 100 nM CDM (pre-mixed) for 15 min before imaging.
2. Dye (ex/em, intensity, pixel dwell time)
TMRE (561/560-630, 1.0 %, 0.89 μ s); CDM (640/640-700, 1.0 %, 0.89 μ s)

The following image shows CDM and TMRE staining at $t = 0$ min (5:49 pm). At this time stamp, mitochondria in cell stay tubular shape. The Pearson's correlation coefficient R value = 0.74. (Objective x20, pixel size = 86 nm^2)

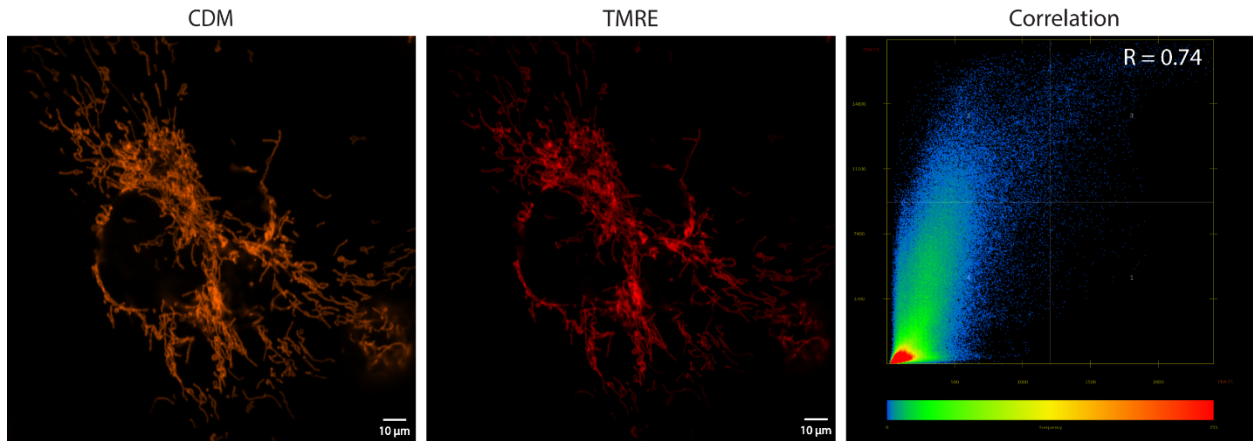


Figure S6. CDM/TMRE overlap. $t = 0$ min. At this time stamp, mitochondria in the cell are still tubular in shape. The Pearson's correlation coefficient R value = 0.74. (Objective x20, pixel size = 86 nm^2).

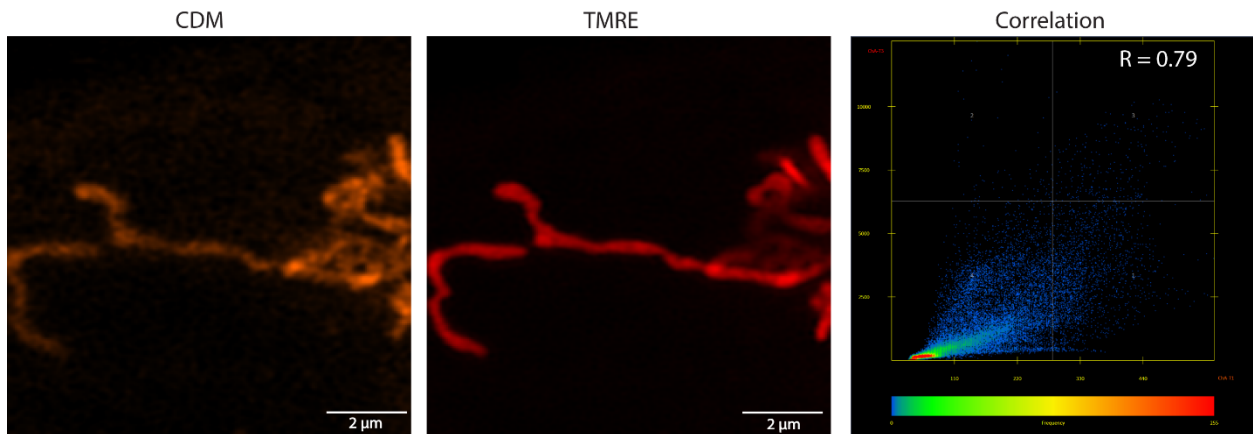


Figure S7. CDM/TMRE overlap. x63 objective used to monitor in detail localization of CDM and TMRE. The Pearson's correlation coefficient R value = 0.79.

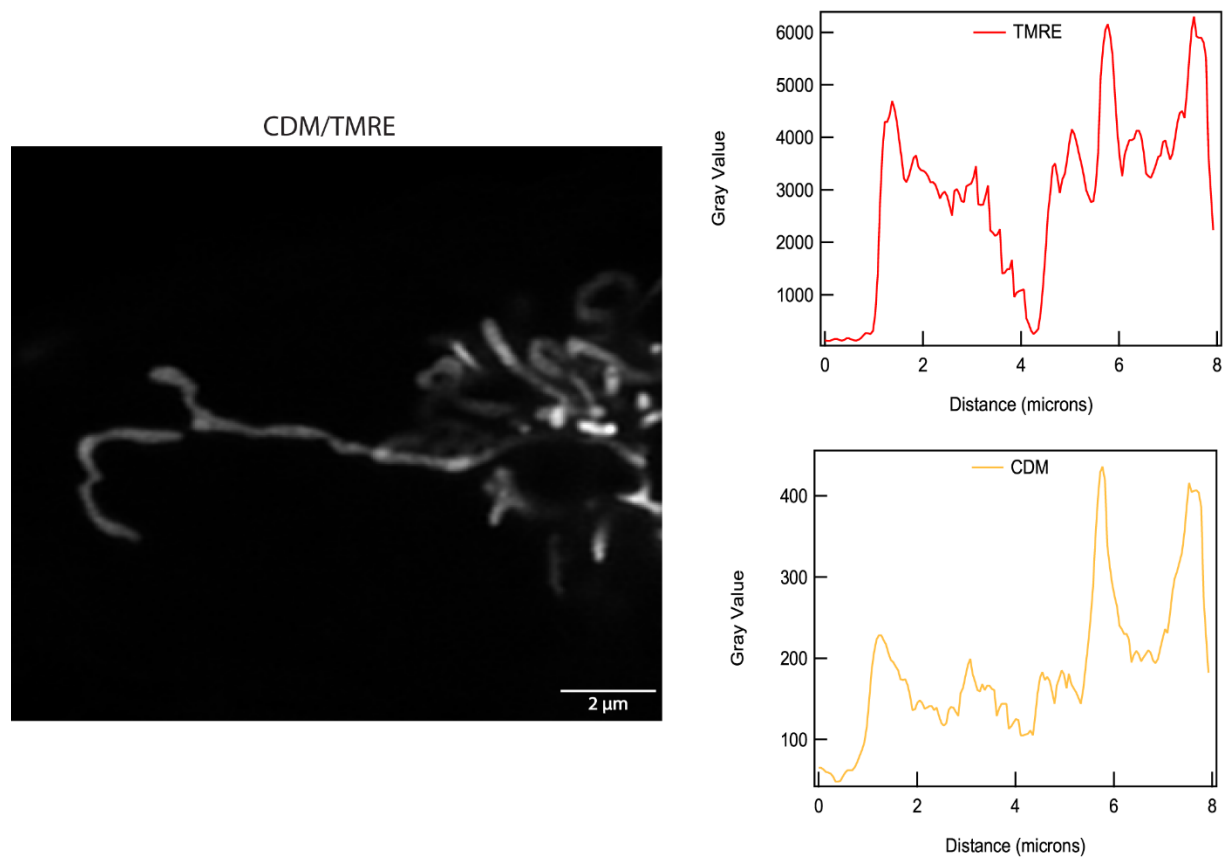


Figure S8. Line profiles of CDM and TMRE images showing colocalization of CDM and TMRE at the mitochondrial cristae.

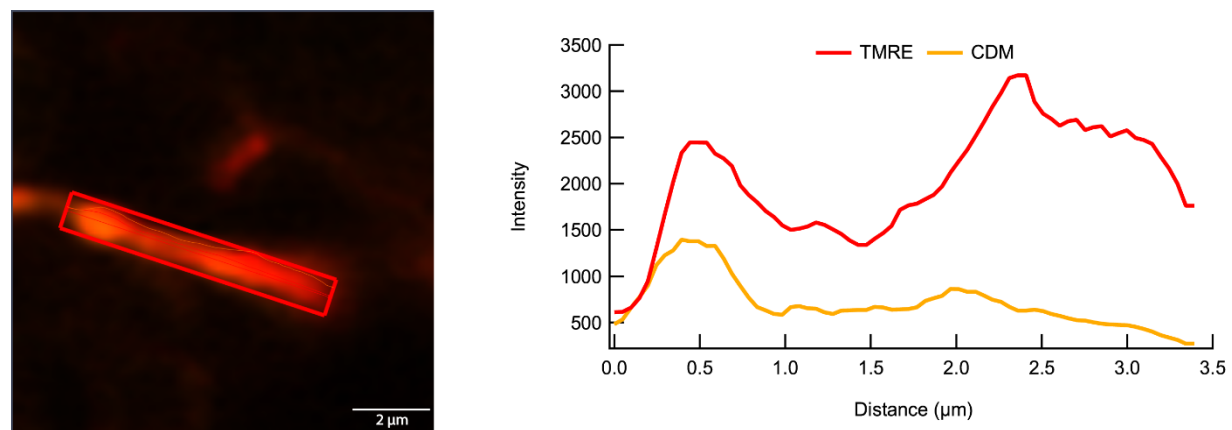


Figure S9. CDM/TMRE overlap images and their line profiles in a separate, independent experiment showing colocalization of CDM and TMRE at the mitochondrial cristae.

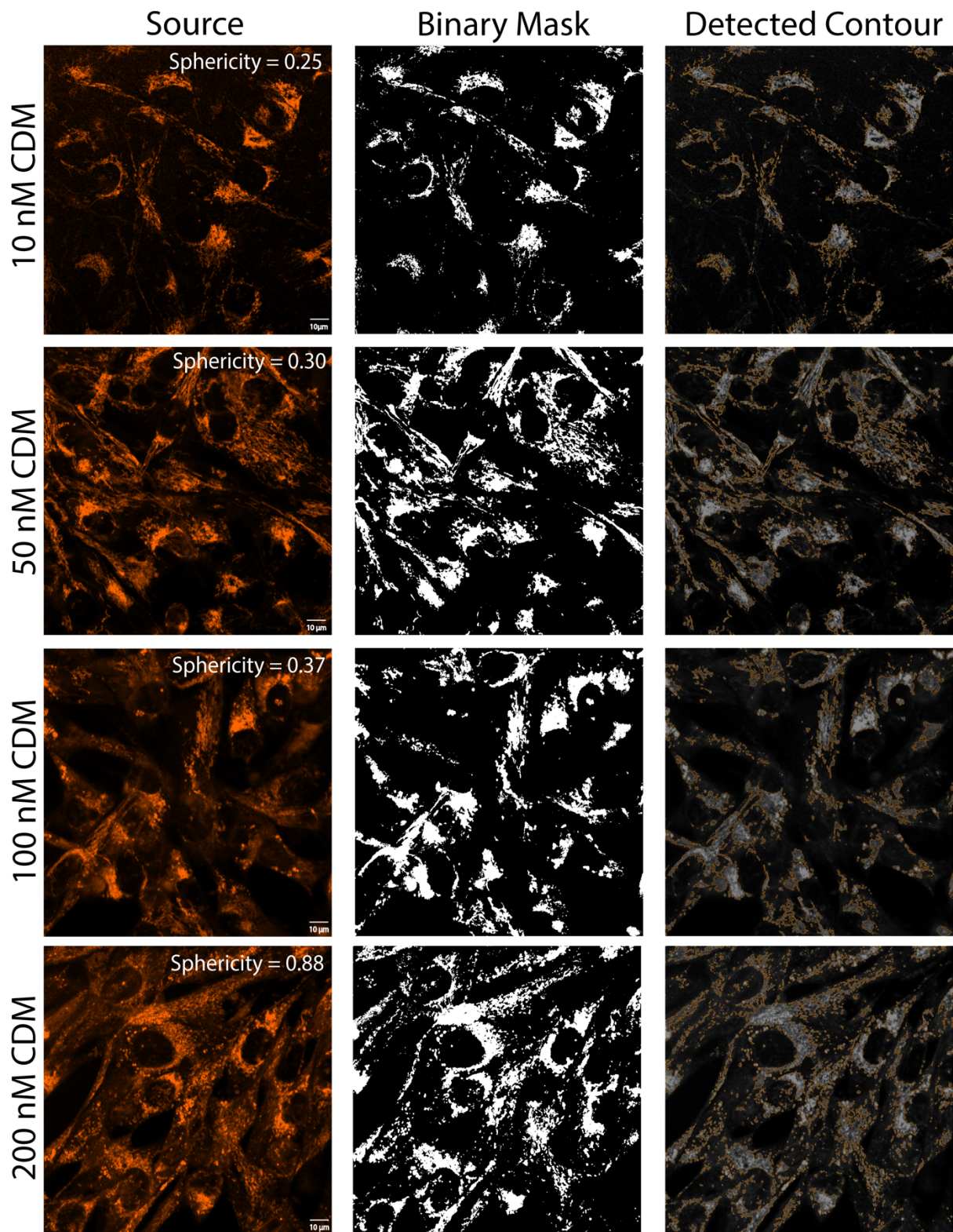


Figure S10. Source, binary mask, and detected contour images used for mitochondrial sphericity titration. MDA-MB-231 cells were incubated with varying concentrations of CDM and imaged after 24 hrs in the CDM channel. Scale bar = 20 μ m.

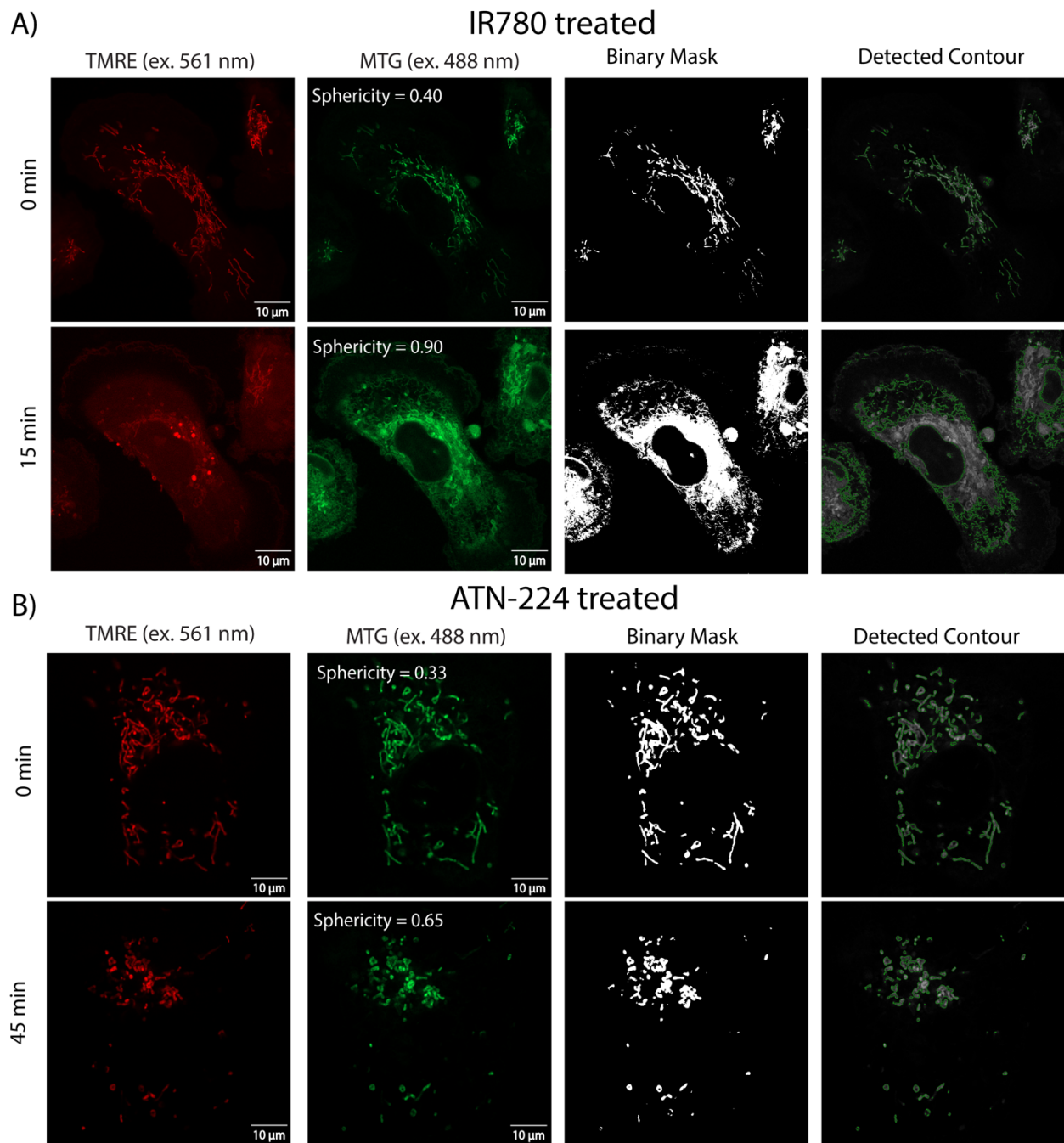


Figure S11. Both IR780 and ATN-224 cause sphericity about IC50. (A) MDA-MB-231 cells were treated with 10 nM TMRE, 10 nM MTG, and then 1 μ M IR780 for 15 minutes. (B) MDA-MB-231 cells were treated with 10 nM TMRE, 10 nM MTG, and then 1 μ M ATN-224 for 45 minutes. Images were obtained in the TMRE (ex. 561 nm, em. 561-700 nm) and MTG (ex. 488 nm, em. 450-561 nm) channels. Each fluorescence image is shown alongside its corresponding binary mask and detected contour representation. Scale bar = 10 μ m.

Figure S11 shows MDA-MB-231 cells stained with 10 nM TMRE and 100 nM MTG to track voltage and morphology, respectively, and incubated with 1 μ M IR780 for 15 min. A significant morphology transformation from tubular to spherical was observed, quantified on average from 0.4 to 0.9. The TMRE fluorescence also decreased from roughly 2000 to 60 arbitrary emission units, indicating a drop in mitochondrial membrane potential.

Another set of cells was incubated with 1 μ M ATN224 for 45 min. During this period, some mitochondria turned into circular shapes with an increase in mitochondrial sphericity from 0.3 to 0.7. The fluorescence signal of TMRE remained the same between time points, suggesting the membrane potential is not impacted by ATN-224 treatment. This trend is supported by cell viability measurements, in which IR780 exhibits a much more potent inhibitory concentration than ATN-224 (12.8 vs >100 μ M, Fig. 6).

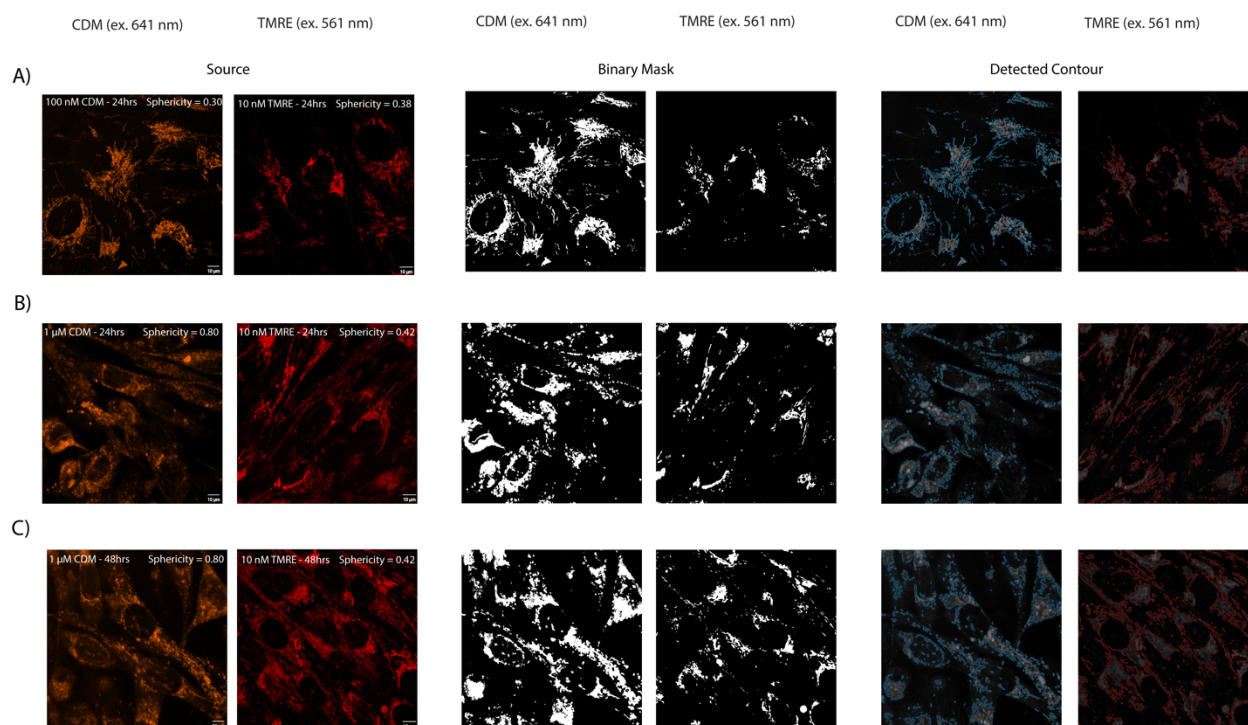


Figure S12. Mitochondrial morphology changes are specific to CDM and irreversible; a control experiment with low concentration TMRE shows no morphology change. (A) MDA-MB-231 cells incubated with 100 nM CDM for 24 hrs demonstrate the same sphericity as cells stained with 10 nM TMRE for 24 hrs. **(B)** MDA-MB-231 cells incubated with 1 μ M CDM for 24 hrs demonstrate a significant change in sphericity compared to 10 nM TMRE. **(C)** MDA-MB-231 cells were incubated with 1 μ M CDM for 24 hrs, then washed and refilled with fresh medium for another 24 hrs. Cells stained with 10 nM TMRE for 48 hrs are used as a control group. Each pair of fluorescence images is accompanied by its corresponding binary mask and detected contour representations. Orange = CDM (ex. 641 nm, em. 642-700 nm). Red = TMRE (ex. 561 nm, em. 561-700 nm). Scale bar = 20 μ m.

To verify the CDM concentration threshold for mitochondrial morphological change, we used 10 nM tetramethyl rhodamine ethyl ester (TMRE) as a control stain. Rhodamines are a well-characterized voltage-sensitive dye for mitochondria (17). In this figure, we only use TMRE as a structure change to observe CDM effect on sphericity. We incubated the MDA-MB-231 cells with 10 to 200 nM CDM for 24 hours and checked the mitochondrial sphericity of each group of cells. The 10 nM, 50 nM, and 100 nM groups demonstrated a sphericity range between 0.2 and 0.5, while the 200 nM group showed a sphericity between 0.8 and 1.0. The concentration threshold for this morphological alteration is around 100 nM to 200 nM

This table summarizes each individual mitochondrion's calculated Area, Perimeter, and Sphericity values corresponding to Figures S10 to S12. We used Binary Segmentation Masks generated with our proprietary algorithm called "mitoAnnotation" (based on the Python programming language) to obtain these measurements. Each segmented image was compared to the original image to ensure its accuracy, and numerical values were obtained using the Analyze Particles tool in ImageJ software. These data are the basis for quantifying representative images and box plots presented in the subsequent figures.

Figure	Treatment	Area (μm^2)	Perimeter (μm)	Sphericity
S10	10 nM CDM-24 hrs	0.13 μm^2	2.56 μm	0.25
S10	50 nM CDM-24 hrs	0.21 μm^2	2.97 μm	0.3
S10	100 nM CDM-24 hrs	0.2 μm^2	2.59 μm	0.37
S10	200 nM CDM-24 hrs	0.48 μm^2	2.62 μm	0.88
S11-A	IR780-0 min	0.0062 μm^2	0.44 μm	0.4
S11-A	IR780-15 min	0.011 μm^2	0.38 μm	0.9
S11-B	ATN224-0 min	0.012 μm^2	0.67 μm	0.33
S11-B	ATN224-45 min	0.015 μm^2	0.54 μm	0.65
S12-A	100 nM CDM-24 hrs	1.41 μm^2	7.77 μm	0.3
S12-A	Control (10 nM TMRE-24 hrs)	2.51 μm^2	9.05 μm	0.38
S12-B	1 μM CDM-24hrs	0.23 μm^2	1.91 μm	0.8
S12-B	Control (10 nM TMRE-24 hrs)	5.27 μm^2	12.17 μm	0.42
S12-C	1 μM CDM-48hrs	0.54 μm^2	2.86 μm	0.8
S12-C	Control (10 nM TMRE-48 hrs)	3.03 μm^2	9.68 μm	0.42

Table S1. Mitochondrial area, perimeter, and sphericity measured under different treatment conditions.

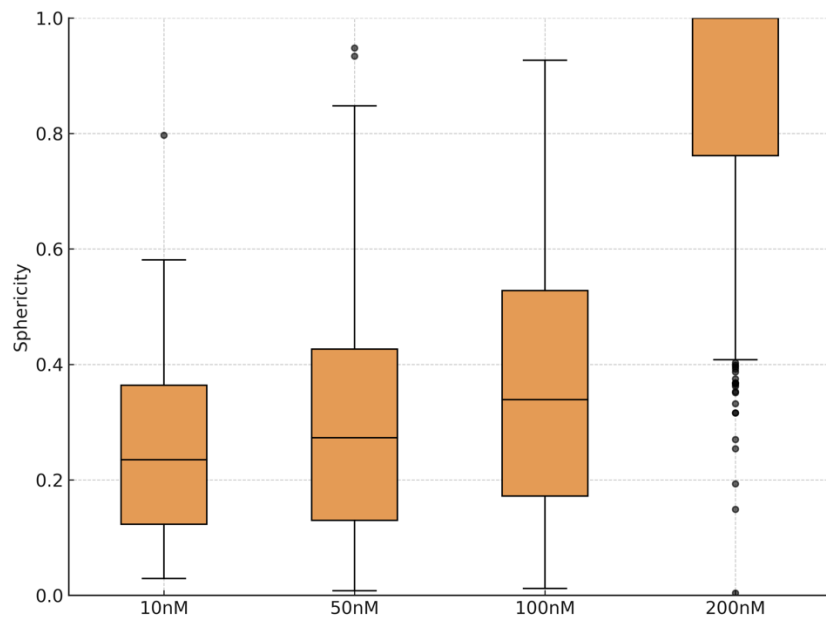


Figure S13. Box plot comparison of mitochondrial sphericity based on Figure S10 segmentations.

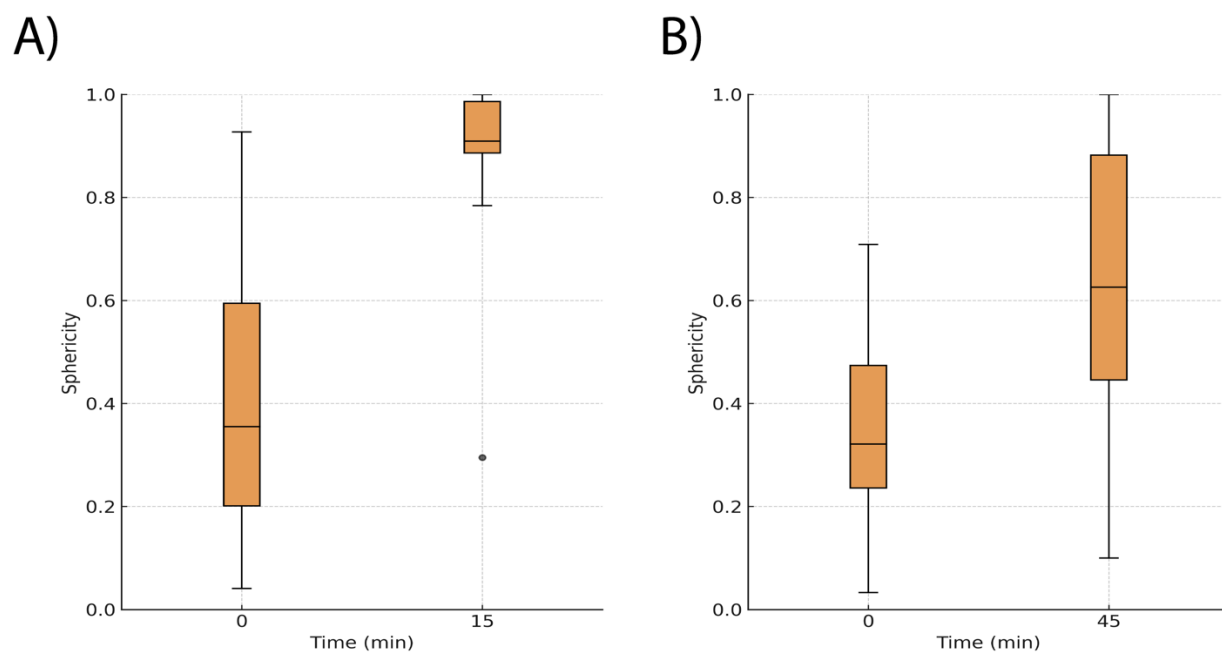


Figure S14. Box plot comparison of mitochondrial sphericity based on Figure S11 segmentations. **(A)** MDA-MB-231 cells were treated with 1 μ M IR780 for 15 minutes. **(B)** MDA-MB-231 cells were treated with 1 μ M ATN-224 for 45 minutes.

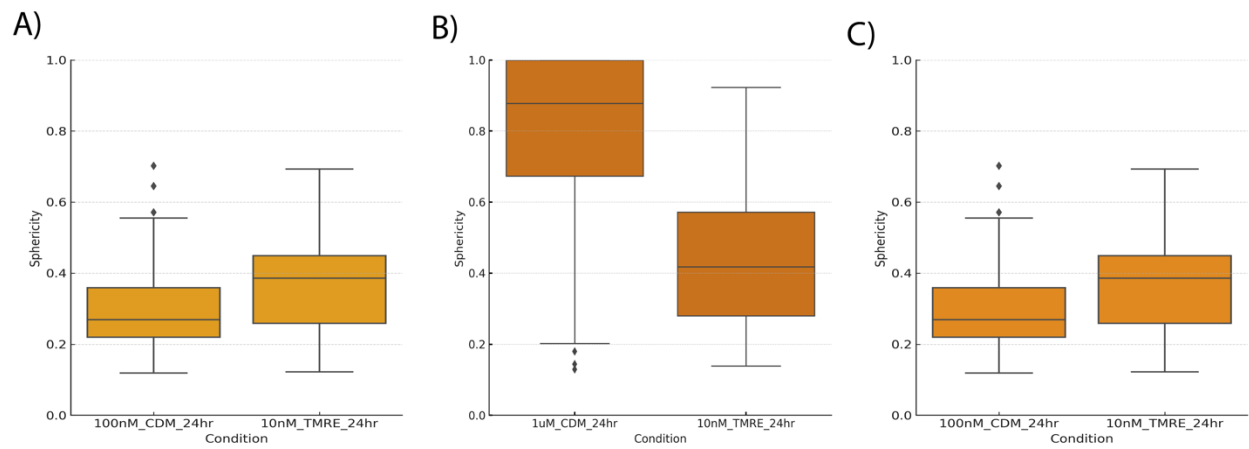


Figure S15. Each condition corresponds to the image sets shown in Figure S12. Data represent the distribution of mitochondrial sphericity for each treatment group. Box plot comparison of mitochondrial sphericity between **(A)** 100 nM CDM and 10 nM TMRE treatments for 24 hrs, **(B)** 1 μ M CDM and 10 nM TMRE treatments for 24 hrs, **(C)** 1 μ M CDM and 10 nM TMRE for 48 hrs.

Figure	Laser Power (mW)	Pixel Dwell Time (μ s)	Total Pixels	Number of Frames	Scan Area (cm^2)	Energy Dose (J/cm^2)	Phototoxicity
2A	0.01	0.58	1019×1025	1	1.93×10^{-5}	0.31	No
2B	0.005	0.84	201×195	1	9.4×10^{-5}	0.16	No
4A	0.01	0.84	1237×623	1	7.4×10^{-5}	0.088	No
4B	0.01	0.84	1242×721	1	8.6×10^{-5}	0.087	No
S2-Control	0.005	0.85	488×488	1	5.5×10^{-5}	0.018	No
S2-10 μ M	0.005	0.66	1326×1452	1	4.62×10^{-5}	0.14	No
S2-50 μ M	0.005	0.85	488×488	1	5.5×10^{-5}	0.18	No
S2-100 μ M	0.005	0.85	488×488	1	5.5×10^{-5}	0.18	No
S3-0 min	0.01	1.28	3246×1688	1	3×10^{-4}	0.23	No
S3-60 min	0.01	1.28	3246×1688	1	3×10^{-4}	0.23	No
S3-120 min	0.01	1.28	3245×1660	1	2.95×10^{-4}	0.23	No
S3-180 minp	0.01	1.28	3278×1678	1	3.01×10^{-4}	0.23	No
S5	0.01	1.15	159×157	1	5.99×10^{-7}	0.48	No
S10-10 nM	0.01	0.84	1247×1267	1	1.52×10^{-4}	0.09	No
S10-50 nM	0.01	0.84	1261×1269	1	1.54×10^{-4}	0.09	No
S10-100 nM	0.01	0.84	1250×1220	1	1.46×10^{-4}	0.09	No
S10- 200 nM	0.01	0.84	1263×1232	1	1.49×10^{-4}	0.09	No
S11-A	0.01	1.15	1810×1810	1	6.06×10^{-5}	0.62	No
S11-B- 0 min	0.01	1.15	1023×982	1	1.86×10^{-5}	0.62	No
S11-B-45 min	0.01	1.15	962×976	1	1.74×10^{-5}	0.62	No
S12-A-CDM	0.03	0.84	830×817	1	6.51×10^{-5}	0.26	No
S12-A-TMRE	0.01	1.47	960×930	1	6.6×10^{-5}	0.2	No
S12-B-CDM	0.03	0.84	850×852	1	6.96×10^{-5}	0.26	No
S12-B-TMRE	0.01	1.47	957×961	1	6.8×10^{-5}	0.2	No
S12-C-CDM	0.03	0.84	852×829	1	6.78×10^{-5}	0.26	No
S12-C-TMRE	0.01	1.47	952×961	1	6.77×10^{-5}	0.2	No
2-0S (Lee et al., 2024)	0.003	3.55	126×126	1	2.8×10^{-7}	0.6	No
2-180S (Lee et al., 2024)	0.003	3.55	126×126	37	2.8×10^{-7}	223.39	Yes
4-1S (Lee et al., 2024)	0.005	1.43	96×96	1	1.63×10^{-7}	0.4	No
4-10S (Lee et al., 2024)	0.005	1.43	96×96	10	1.63×10^{-7}	4.05	Yes

Table S2. Calculation of illumination energy doses for imaging experiments in the current study compared to previously established phototoxicity thresholds (21,33). All values were computed based on acquisition parameters and are reported in J/cm^2 . The results confirm that all imaging was performed below the levels known to cause phototoxic effects.

Energy doses were estimated using the following formula (assuming uniform illumination across the scanned region):

$$\text{Energy Dose (J/cm}^2\text{)} = (\text{Laser Power (W)} \times \text{Pixel Dwell Time (s)} \times \text{Total Number of Pixels} \times \text{Number of Frames}) / \text{Scan area (cm)}^2$$

Phototoxic thresholds vary depending on the fluorophore and imaging conditions. A value of ~ 2 J/cm² has been reported for MitoTracker Red (CMXRos) (33), while more recent studies (21) confirmed that dyes such as MitoTracker Green (MTG) and TMRE show significantly lower phototoxicity and remain stable even under prolonged imaging.

Table S2, shows that the light conditions we used in our experiments are well below this threshold. This confirms that the changes in mitochondrial shape we observed are due to the chemical effect of CDM and not to phototoxicity caused by imaging.

Detailed Image Analysis and Quantification Procedures for Figure 5

1. Length, Width, and Branching Count Analysis

Mitochondrial length, width, and branching count were measured using ImageJ software. Briefly, fluorescence images were first converted to a binarized state by automatic thresholding (Otsu method (66)). Then, the particle analysis tool measured mitochondrial sizes (length and width). We used the skeletonization method to obtain the branching count and then calculated it using the Analyze Skeleton plugin in ImageJ. Binary mask, detected contour, and skeletonized images used for these analyses are presented in Figure S16. The numerical values of length, width, and branching count in each experimental condition are summarized in Table S3. Cells treated with copper had a greater mean mitochondrial length (5.76 px vs. 4.93 px), greater width (4.32 px vs. 3.89 px), and significantly greater number of branches (210 vs. 90) than the No copper group. These results indicate that exogenous copper increases the length and remodels mitochondrial networks, ending the fragmented state caused by copper depletion.

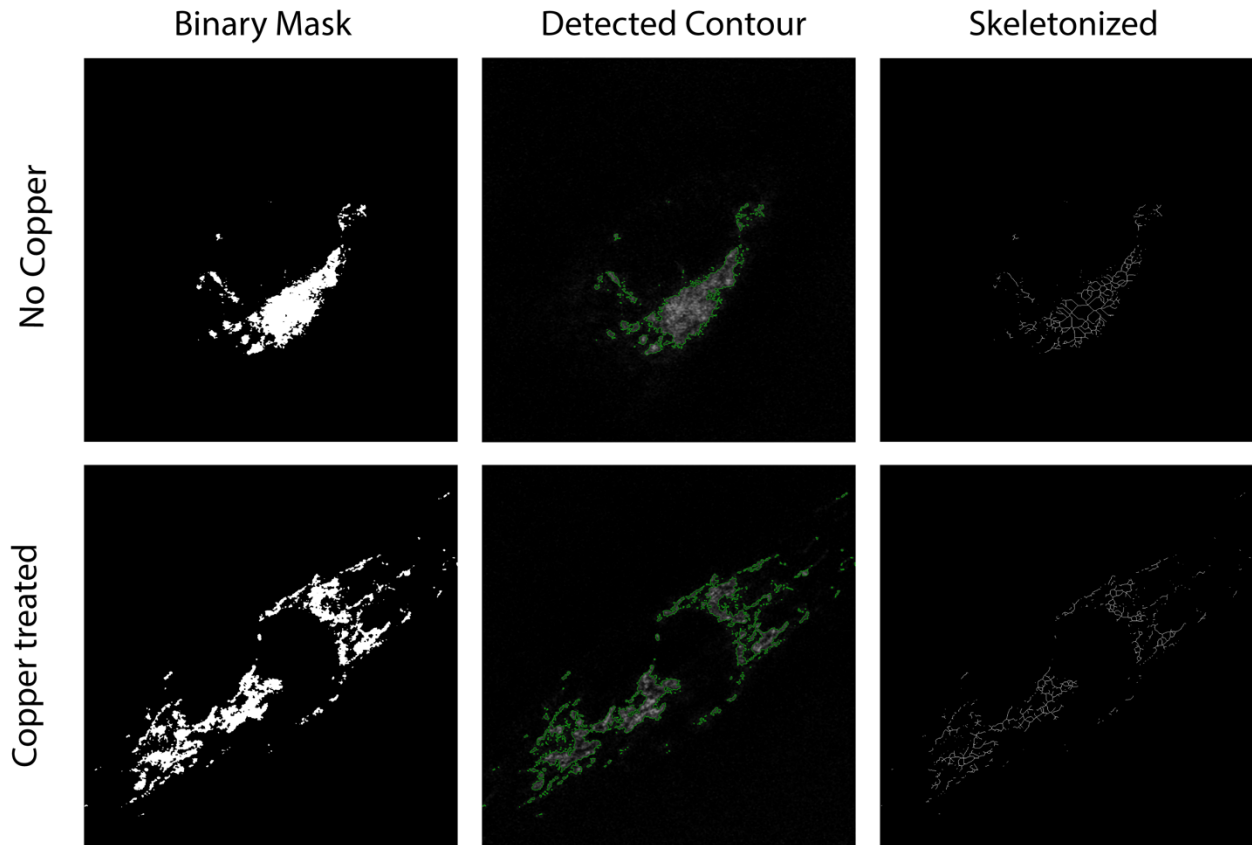


Figure S16. Representative image processing steps used mitochondrial morphology analysis for No copper and Copper-treated groups.

Figure	Mean Length (px)	Mean Width (px)	Branching Count
No Copper	4.930	3.890	90
Copper treated	5.760	4.320	210

Table S3. Quantitative image analysis.

2. Sphericity Calculation

The measured values of mitochondrial area, perimeter, and sphericity for each experimental condition are given in Table S4. Compared to the No copper group, which had a mean sphericity of 0.75, copper-treated cells showed a significant decrease in sphericity (0.16). This decrease indicates that mitochondria have changed shape towards more elongated and filamentary structures. This change is consistent with the restoration of healthy mitochondrial morphology after copper replacement.

Figure	Area (μm^2)	Perimeter (μm)	Sphericity
No Copper	0.3 μm^2	2.29 μm	0.75
Copper treated	6.29 μm^2	22.24 μm	0.16

Table S4. Morphological shape descriptors.

3. Statistical Analysis

Statistical comparisons between the No-copper and Copper-treated groups were performed using the nonparametric Mann-Whitney U test in GraphPad Prism version 10.2.2. This test was chosen because the mitochondrial morphology data were not normally distributed. Box plots were also drawn for length, width, branching count, and sphericity using the same software (Figure S17 and Figure S18). These analyses considered statistical significance when the p-value was less than 0.05.

The p-values obtained are summarized in Table S5 and show that there was a statistically significant difference in mitochondrial length ($p = 0.022$), a borderline difference in width ($p = 0.049$), and a highly significant difference in branching ($p = 1.59 \times 10^{-5}$) between the two groups.

Condition Compared	Metric	p-Value (Mann-Whitney U)
No Copper vs. Copper Treated	Length	0.022
No Copper vs. Copper Treated	Width	0.049
No Copper vs. Copper Treated	Branching Count	1.59×10^{-5}
No Copper vs. Copper Treated	Sphericity	1.77×10^{-4}

Table S5. Statistical comparison of morphology.

Figure S17 shows box plots comparing mitochondrial morphology features, including A) length, B) width, and C) branching count. These plots show that all three features increased after copper treatment; this increase is consistent with the expected restoration of mitochondrial structure after treatment.

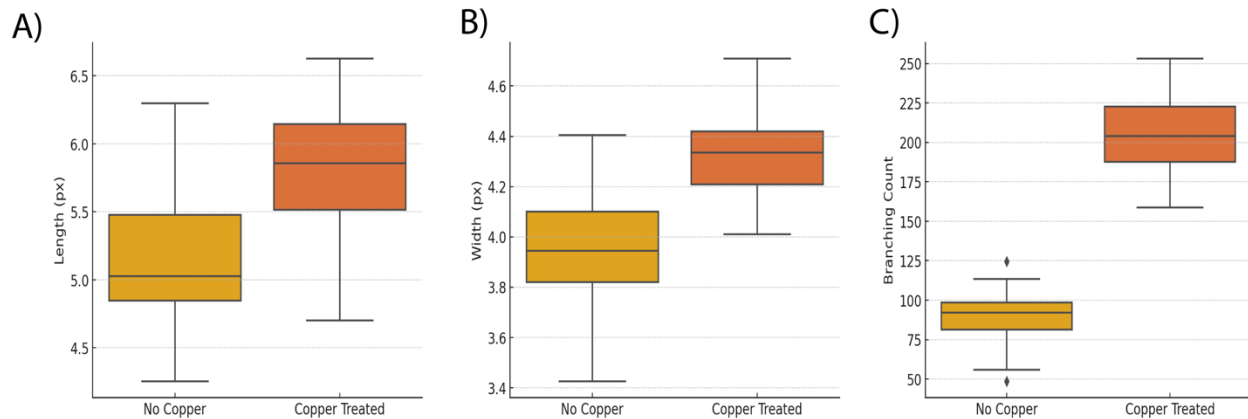


Figure S17. Box plot comparison of mitochondrial morphology features. (A) Length, (B) Width, (C) Branching count for No copper and Copper-treated conditions.

Figure S18 shows a box plot comparison of mitochondrial sphericity between the No-copper and Copper-treated conditions. In the Copper-treated group, the sphericity value was significantly reduced. This reduction indicates that mitochondria have changed from round and fragmented to elongated and filamentous structures. This change is consistent with the morphological recovery of mitochondria.

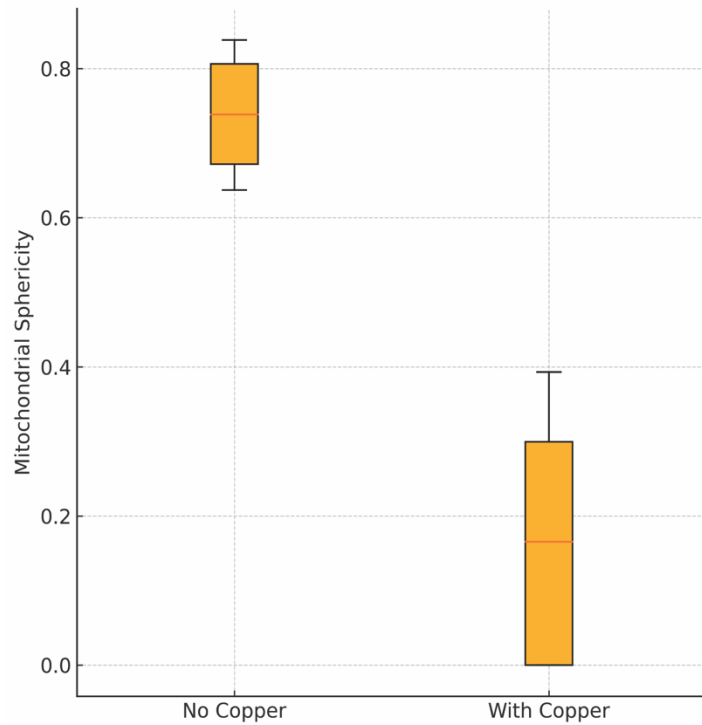


Figure S18. Box plot comparison of mitochondrial sphericity between No copper and Copper-treated conditions.

Figure S19 shows the kinetics of CDM's release rate and efficiency from CDN. CDN in buffers with different pH values at 37 °C. At the indicated time, CDN was collected using a centrifuge filter and redispersed in 50 mM HEPES buffer for fluorescent measurement. The loss of fluorescent signals is due to the release of CDM. In an acidic condition with a pH of 4.5, which is close to the environment in lysosomes, CDM was rapidly released from CDN, with a half-life of around 10 min. The fast release of CDM in acidic conditions contributed to the migration of CDM from lysosomes and further accumulation in the mitochondria. At a higher pH level of 5.5, the release rate was vastly reduced with a half-life of about 22 min. At neutral pH, there was a 35% loss in the fluorescent signal after 1 h. It was also noted that at lower temperatures, the releasing rate of CDM from CDN was also reduced, with a half-life of 30 min and 55 min at 25 °C and 4 °C, respectively.

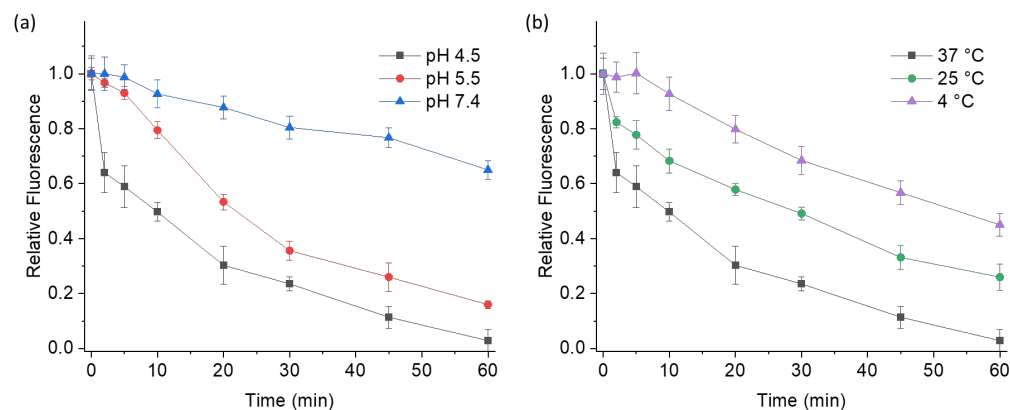


Figure S19. (a) The relative fluorescent signals of CDM in different pH conditions at 37 °C, and **(b)** the relative fluorescent signals to varying temperatures in a buffer with a pH of 4.5. The concentration of CDM is 1 μ M.